International Reviews in Physical Chemistry
Vol. 00, No. 00, March 2014, 1–36

Review

Path Integral Monte Carlo investigations on doped helium clusters

Rocío Rodríguez-Cantano, Tomás González-Lezana* and Pablo Villarreal

IFF-CSIC, Serrano 123, 28006 Madrid, Spain;

(*2015*)

One of the most commonly employed methods to study doped helium clusters is the Path Integral Monte Carlo (PIMC) approach. In this review we present results of recent investigations on a series of both atomic and diatomic dopants attached to droplets formed with up to 40 He atoms. Besides the comparison with similar studies existing in the literature, this work also gives the possibility to analyse different issues such as the role played by the He–impurity interaction in the overall geometry of the clusters, the inclusion of internal molecular degrees of freedom and the exchange permutation symmetry in the PIMC calculations. The study of the structure and energies of $He_N Ca$, $He_N Rb_2$, $He_N He^{*-}$ and $He_N He_2^{*-}$ at thermal equilibrium presented in this work thus covers most of the usual aspects treated for these kinds of doped systems.

Contents

*Email: t.gonzalez.lezana@csic.es

ISSN: print/ISSN online

DOI:
http://www.tandfonline.com

1. Introduction

Due to its unique properties, helium constitutes an ideal environment for spectroscopic measurements of a broad range of different embedded dopants [1–11]. Since the pioneering vibrational spectroscopy of SF_6 attached to helium clusters [12], the first system for which both rotationally resolved spectrum and droplet temperature were experimentally obtained [13], helium nanodroplets have been found as perfect candidates to host atomic and molecular species to investigate. As a liquid, helium can undergo a phase transition to a superfluid state at $T = 2.18$ K for the ^{4}He isotope and $T = 3 \times 10^{-3}$ K for ^{3}He, a property which has been widely exploited to probe the main rotational features of various systems at a low temperature regime. These optimum temperature conditions and the possibility of a frictionless matrix to embed molecular species has made superfluidity in small and nanodroplets the goal of an extense literature [5, 14–17]. Calculation of effective rotational constants, definition of models assuming adiabatic following of the helium layers around the rotating dopant and the analysis of the number of He atoms participating in exchange permutation paths or the analysis of superfluid fractions have been developed as useful indicators to probe this unsual character of doped helium clusters. The interested reader can find a complete review of theoretical techniques developed to investigate superfluidity for both helium and para-H_2 clusters in Ref. [18].

One of the most investigated issues in these kinds of systems regards the position of the impurity with respect to the helium cluster. A possible way to infer this aspect consists on the comparison between the absorption or Raman spectra obtained from the doped droplet with the corresponding measurements in either the gas phase or bulk. Shifts and widths of the corresponding transitions can be good indicators of the cluster geometry and the position of the embedded species, although in some cases contradictory conclusions have been reported for the same system. Thus for example the location of SF_6 contained in clusters made of few thousand He atoms was originally supposed near the surface from infrared spectrum [12] whereas a subsequent rotationally resolved spectroscopic study concluded that the dopant was located inside the droplet [13]. Investigations on atomic impurities on helium clusters also reveals a rich variety of possibilities: While Ag gets trapped inside a solvating environment [19], alkaline atoms (Li, Na or K) seem to be located at dimples at the surface [20–23]. Predictions for alkaline earth however are in principle more uncertain. Since the observed electronic spectra for Ca [24], Sr [24] and Ba [25] attached to helium clusters are broader blue-shifted than those reported for alkaline, the possibility of immersion or formation of inside bubbles has been suggested. The smaller shift to the blue in comparison with the spectra for the bulk helium leads to propose the location of the dopant in the region of low helium density close to the surface [4]. Mg, in turn, constitutes a frontier example between surface location and solvation [26, 27].

Diatomic impurities such as Li_2 [28], Cs_2 [29] or Rb_2 [30, 31] exhibit very weak binding energies to helium clusters. As a result, recent investigations have revealed the preference of these dopants to site at certain distance outside the droplet, with different possibilities for the orientation of the molecular axis with respect to it. In fact a precise description between the impurity and He is crucial for a correct characterization of the geometry of doped clusters. For the case of an atomic dopant,

Ancilotto *et al.* [32] developed a simplistic model based on the well depth and the equilibrium internuclear distance of such interaction described by Lennard-Jones potentials. According to the value of a dimensionless parameter, with a threshold value of $\lambda_A = 1.9$, predictions regarding the solvation of a specific dopant could be established. For the above mentioned cases of Mg and Ca, different conclusions were obtained for existing He–Mg [33, 34] and He–Ca [33, 35] interaction potentials, and solvation within the helium medium was discussed in each case depending on the values of the model parameter [26]. At the other extreme, van der Waals dihalogen dopants such as I_2 [36–38], Cl_2 [39], ICl [40] or Br_2 [41, 42] present a much stronger interaction with He, and consequently the corresponding doped systems formed with helium droplets contain the impurity embedded in the interior [36].

The above mentioned location of the dopants outside of the helium clusters in most of the cases is one of the reasons why superfluidity has not usually been among the main goals in previous investigations on the systems treated in this review. Under these configurations the dopant has an almost negligible effect on the supefluid properties of the helium cluster. Thus, for instance, being Rb_2 at the top of a He surface in the study by Guillon *et al* [30], and due to the large stochastic noise in the corresponding calculations, the study of the possible local nonsuperfluid fraction below the Rb_2 molecule introduced in the helium environment was not possible. Analogously, alkali atoms trapped in helium clusters have been only related to superfluid features within the context of quantized vortices. In particular, barely stable atoms in a dimple state on the surface becomes solvated inside the cluster in the presence of a vortex, which in essence can be understood as an excited state of a superfluid system [43].

Besides theoretical methods to calculate the corresponding interparticle interactions [44], different approaches have been employed to investigate both energetics and structures of the clusters. Monte Carlo (MC) [16, 45–53], quantum chemistry-like [40, 54–58] and density functional techniques [59, 60] have been developed along the years as useful approaches to tackle the study of these systems. In particular, path integral MC (PIMC) is perhaps the most commonly used method for both pure and doped helium clusters at finite temperature [61–63]. Dynamical and structural properties of a long list of small and medium doped clusters formed with dopants such as C_6H_6 [16], CO_2 [64], N_2O [53, 65], OCS [16, 66] or SF_6 [67, 68] have been analyzed by means of this method.

This work comprises PIMC investigations on a series of doped helium clusters performed in our group over these past years. Special emphasis is given to the potential energy surfaces (PESs) describing the interactions between the components of the species under study. Thus, the case of Ca is used to carry out a detailed comparative analysis between results obtained with two existing He–dopant interactions which lead to different energies and geometries for He_NCa. The potential energy interactions in some of the systems here considered, on the other hand, are taken from previously reported analytical functions in the literature and numerical fittings over existing *ab initio* energies. Finally, ionic dopants such as He^{*-} and He_2^{*-}, recently investigated as possible candidates, especially the atomic anion, to participate as charge carriers within a helium environment, have been taken into account. The in-

clusion of diatomic species in this work allows us to present examples with a specific treatment of the impurity's internal degrees of freedom such as rotation within the PIMC framework.

The review is structured as follows: First, in Section 2 basic details about the theory of the PIMC method, relevant to the present calcul ations are shown; then numerical details and results for the He_N–Ca, He_N–Rb_2, He_N–He^{*-} and He_N–He_2^{*-} systems are given en Sections 3, 4, 5 and 6, respectively. In Section 7 final conclusions are discussed.

2. Theoretical Method: The PIMC approach

A full description of the PIMC method can be found in previous works [63, 69–71] so here we will only refer to the most relevant details. According to this approach the thermal average of a quantum observable $\hat{A}$ is obtained as

$$\hat{A} = Z^{-1} \int d\mathcal{R} d\mathcal{R}^{'} \rho(\mathcal{R}, \mathcal{R}^{'}; \beta) \langle \mathcal{R} | \hat{A} | \mathcal{R}^{'} \rangle, \tag{1}$$

where Z is the partition function, $\beta = 1/k_B T$ and the density matrix at a temperature T, defined as $\rho(\mathcal{R}, \mathcal{R}'; \beta) = \langle \mathcal{R}' | e^{-\beta \hat{H}} | \mathcal{R} \rangle$, can be replaced by the product of M density matrices at a higher-temperature $T' = T \times M$ as follows:

$$\rho(\mathcal{R}_0, \mathcal{R}_M; \beta) = \int d\mathcal{R}_1 \dots d\mathcal{R}_{M-1} \prod_{\alpha=0}^{M-1} \rho(\mathcal{R}_\alpha, \mathcal{R}_{\alpha+1}; \tau). \tag{2}$$

In Eq. (2) we have defined the discrete-time path as $\tau = \beta/M$, the time step of the path integral. $\mathcal{R}_\alpha$ corresponds to the position vectors of the $\mathcal{N}$ particles of the system: $\mathcal{R}_\alpha \equiv \left\{ \mathbf{r}_1^\alpha, \dots, \mathbf{r}_\mathcal{N}^\alpha \right\}$.

In order to take into account the bosonic character of the N ^{4}He atoms, the density matrix is symmetrized by summing over all permutations $\mathcal{P}$ of the particle labels [69]:

$$\rho_B(\mathcal{R}, \mathcal{R}'; \beta) = \frac{1}{N!} \sum_{\mathcal{P}} \rho(\mathcal{R}, \mathcal{P}\mathcal{R}'; \beta). \tag{3}$$

Under certain circumstances, such as a sufficiently high temperature [29, 61, 63] or low coverage densities of helium over the corresponding molecular substrate [16, 72–77], one might discard for simplicity an explicit inclusion of the identical particle symmetry in ρ.

A general expression of the total Hamiltonian $\hat{H}$ under the primitive approximation [78] must contain terms for the kinetic energy operators $\hat{T}$ and for the potential energy operator $\hat{V}$:

$$\hat{H} = \hat{T} + \hat{V} \tag{4}$$

where $\hat{T}$ can be expressed as:

$$\hat{T} = \hat{T}_\mathrm{X} + \hat{T}_\mathrm{He} = -\frac{\hbar^2}{2m_\mathrm{X}} \nabla^2 - \frac{\hbar^2}{2m_\mathrm{He}} \sum_{i=1}^{N} \nabla_i^2, \tag{5}$$

$\hat{T}_{\rm X}$ being a term due to the impurity and $\hat{T}_{\rm He}$ the contribution from the He atoms; $m_{\rm X}$ is the mass of the impurity and $m_{\rm He}$ the mass of the He atom. $\hat{T}_{\rm X}$ is usually neglected in case of heavy dopants which are assumed effectively as static [29, 66, 69]. $\hat{V}$, on the other hand, comprises the potential energy of the interaction of each He atom with the impurity X and with the rest of He. The specific expression of each of these terms depends on the particular choice of coordinates between the He atoms and the impurity X.

The energy of the system can be obtained by means of the *thermodynamic* estimator developed by Baker [79], expressed as:

$$\langle E\rangle_{\rm thermo} = \frac{3\mathcal{N}}{2\tau} - \left\langle \sum_{\alpha=0}^{M-1}\sum_{i=1}^{\mathcal{N}} \frac{(\mathbf{r}_i^{\alpha}-\mathbf{r}_i^{\alpha+1})^2}{4M\lambda_m\tau^2} - V, \right\rangle \tag{6}$$

where $\mathbf{r}_i^{\alpha}$ is the position vector of the i-th He atom in the α bead, $\langle\rangle$ means average over the MC steps and $\lambda_m = \hbar^2/2m$, with m referring either to He or the impurity as a rigid rotor. The first term in Eq. (6) refers to the classical kinetic energy multiplied by the number of beads M. The second term accounts for the quantum mechanical (QM) energy due to the spring-like interaction assumed between consecutive beads in the same ring describing a specific particle. The last term contains the potential energy $V_{\rm pot}$ as specified in the last two terms of Eq. (4) averaged on M.

Another possible energy estimator is based on the virial theorem [80, 81] and can be expressed as:

$$\langle E\rangle_{\rm virial} = \frac{3\mathcal{N}}{2\beta} - \left\langle \frac{1}{2M}\sum_{\alpha=0}^{M-1}\sum_{i=1}^{\mathcal{N}} (\mathbf{r}_i^{\alpha}-\mathbf{r}_i^{\rm C})\cdot\mathbf{F}_i^{\alpha} - V \right\rangle, \tag{7}$$

where $\mathbf{r}_i^{\rm C} = M^{-1}\sum_{\alpha=0}^{M-1}\mathbf{r}_i^{\alpha}$ defines the centroid of the M beads for the i-th particle. The first term in Eq. (7) accounts for the classical kinetic energy, the second one is a quantum correction where $\mathbf{F}_i^{\alpha}$ is the force experienced by the i-particle on the α slice, defined via the gradient of the potential.

Internal degrees of freedom of the dopant, such as for example the rotation [66, 82, 83], can be also explicitly included in the above formalism. The kinetic energy of the impurity, $\hat{T}_X$, of Eq. (5) includes then a term as:

$$\hat{T}_X^{\rm rot} = B\hat{L}^2, \tag{8}$$

where $\hat{L}$ is the rotational angular momentum of the molecule and B its rotational constant. In the particular case for rigid tops applied to symmetric linear molecules the rotational propagator between the bead α and $\alpha+1$ within the rigid rotor approximation can be expressed as [66, 82, 84, 85]:

$$\rho_{\rm rot}^{\alpha,\alpha+1}(\Omega^{\alpha},\Omega^{\alpha+1};\beta) = \sum_{l=0}^{\infty}\frac{2l+1}{4\pi}\mathcal{P}_l(cos\theta)e^{-\beta Bl(l+1)/M}, \tag{9}$$

where $\mathcal{P}_l$ is a Legendre polynomial, l the quantum number associated with the angular momentum of the impurity and Ω collects the Euler angles in the laboratory frame

[66, 86]. The functional form for the rotational part in the energy estimator is written then as [82, 87]:

$$\langle E\rangle_{\rm rot} = \left\langle \frac{1}{M}\sum_{\alpha=0}^{M-1}\left[\rho_{\rm rot}^{\alpha,\alpha+1}\right]^{-1}\sum_{l=0}^{\infty}\frac{2l+1}{4\pi}Bl(l+1)\mathcal{P}_l(cos\theta)e^{-\beta Bl(l+1)/M}\right\rangle. \quad (10)$$

Depending on the system under study and the temperature for the PIMC calculations it is frequent to impose confinements to prevent evaporation of He atoms from the droplet induced by the corresponding thermal excitations. The usual procedure is to restrict the movement of the atoms inside a sphere centered at either the dopant (in case this is atomic) or, in case of more than one atom, its center of mass (CM), and additionally to limitate the interparticle distances between He atoms in order to prevent the droplet fragmentation.

In an attempt to maximize the efficiency of the PIMC calculation, the simulations are initiated from the geometries obtained by means of the classical MC (CMC) calculation performed with $M = 1$. These, in turn, can be the result of optimizations from the structures obtained from the exploration of the PES in search for the absolute minimum performed with an evolutive algorithm (EA) [88]. This procedure usually The calculations usually involve between 10^6 and 10^8 MC steps, with a number of beads M which varies between 50 and 500 depending on the size of the cluster under study. A Metropolis algorithm [89] is employed in internal and translational degrees of freedom, completed with either the staging method or a multilevel Metropolis method [61, 63, 90] for the latter case [91]. The average energy for each $He_N X$ system can be obtained by extrapolating τ to 0 (that is, M to ∞) following a parabolic law [29, 66, 92].

Information regarding the structure and geometry of the corresponding clusters can also be obtained by means of the radial probability density function for the He–He distance:

$$\mathcal{D}_{\rm He}^{(N)}(r_{\rm He-He}) = \frac{2}{N(N-1)M}\left\langle\sum_{\alpha=0}^{M-1}\sum_{i<j}^{N}\delta(r_{\rm He-He}-r_{ij}^{\alpha})\right\rangle \quad (11)$$

and for the distance between the He and the dopant impurity X as follows:

$$\mathcal{D}_{\rm X}^{(N)}(r_{\rm He-X}) = \frac{1}{NM}\left\langle\sum_{\alpha=0}^{M-1}\sum_{i=1}^{N}\delta(r_{\rm He-X}-\mid \mathbf{r}_i^{\alpha}\mid)\right\rangle. \quad (12)$$

Analogously, the angular distribution for $\cos\gamma$, with γ the angle formed between two He position vectors $\mathbf{r}_i^{\alpha}$ and $\mathbf{r}_j^{\alpha}$, is calculated as:

$$\mathcal{D}_{\gamma}^{(N)}(\cos\gamma) = \frac{2}{N(N-1)M}\left\langle\sum_{\alpha=0}^{M-1}\sum_{i<j}^{N}\delta(\cos\gamma-\mid \mathbf{r}_i^{\alpha}\cdot\mathbf{r}_j^{\alpha}\mid)\right\rangle, \quad (13)$$

and, in the case of a diatomic impurity the corresponding to $\cos\theta$, with θ describing the angle formed between the position vector of one He atom, $\mathbf{r}_i^{\alpha}$, and the diatom axis, can be written as:

$$\mathcal{D}_{\theta}^{(N)}(\cos\theta) = \frac{1}{NM}\left\langle \sum_{\alpha=0}^{M-1}\sum_{i=1}^{N}\delta(\cos\theta - \cos\theta_i^{\alpha})\right\rangle . \tag{14}$$

3. He_N-Ca

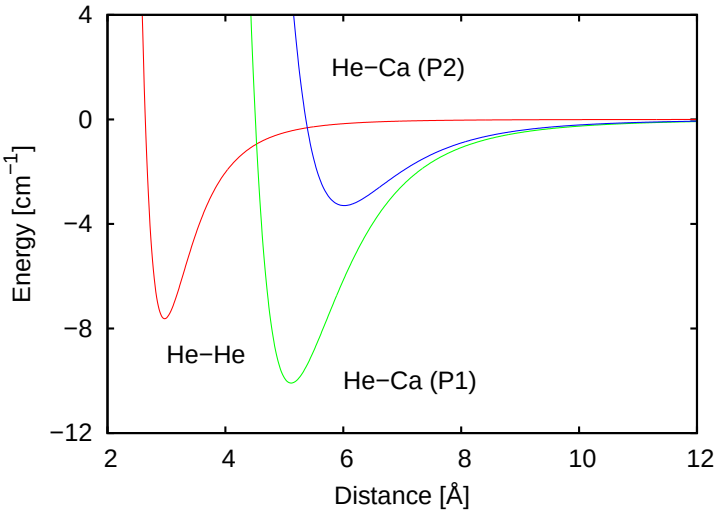

Figure 1. Pair potential energy interactions (in cm^{-1}) used in the PIMC calculation for the He_NCa clusters. The He-He potential (red) has been taken from Ref. [93], and for the He-Ca interaction, P1 potential (green) corresponds to Ref. [94] and P2 potential (blue) to Ref. [95]. See text for details.

The He–Ca interaction has been the subject of numerous theoretical studies. Most of the available potentials on the literature can be classified in two main groups: (i) models developed by means of semi empirical formulations [94, 96] and (ii) *ab initio* potentials [26, 35, 95, 97–99]. Properties such as the equilibrium distance and the potential well differ depending on the specific potential. In particular, comparative investigations of binding energies and structures for the He_2Ca trimer [100, 101] by using one potential from each type [94, 95] revealed noticeable differences in the simulated infrared spectra [101]. For much larger clusters, the position of the dopant with respect to the helium droplet has motivated interesting discussions [4, 24]. The measured blue shift ($\sim$ 70 cm^{-1}) in electronic absorption spectra of Ca atoms attached to the He_N cluster [24, 102] has been generally explained assuming that the impurity stays at the surface of the droplet. This feature has motivated a preference in theoretical calculations for those potentials with a weaker interaction between He and the Ca atom. The analysis of some of these interactions by means of the above mentioned Ancilotto's model [32] yields different predictions with respect to the solvation of the impurity inside the helium cluster. Thus for example, the self consistent field/configuration interaction potential of Ref. [35] yields a value of the model parameter $\lambda_A = 2.1$, just slightly above the threshold value of 1.9, whereas for the potential

reported in [94], $\lambda_A = 5.5$ and therefore clearly in favour of an immersed dopant. On the contrary, weaker He-Ca interactions such as the Hartree-Fock damped dispersion potential calculated in Ref. [26] leads to $\lambda_A = 1.4$ thus suggesting that the impurity may be located outside the cluster. Despite calculations employing such potentials certainly predict such location of the dopant, some intriguing aspects remain unclear. Thus despite the minimum energy configuration predicted by density functional calculations is a dimple state at the surface, the difference with respect a solvated state is less than ~ 10 cm^{-1} [60], certainly a small value in comparison with the energy associated to the absorption frequency of the calcium atoms ($\sim 23,600 - 23,700$ cm^{-1}). In fact, the precise calculation of electronic excitation spectra of Ca-doped He clusters require accurate potentials for both the ground and excited electronic He–Ca potentials [35, 98, 99, 103, 104].

One of the issues treated on the theoretical studies of these systems deals with the specific isotopic composition of the He cluster [60, 99, 102, 104]. Indications of a different geometry for the case of the trimer [100] depending on the presence of ^{3}He and ^{4}He were somehow corroborated with the behaviour observed for systems of larger sizes. In particular pure ^{3}He clusters completely solvate the Ca atom but with a proper combination of atoms of each isotope it is possible to see how the dopant penetrates the fermionic shell reaching the inner ^{4}He core. These isotopic differences were also observed in laser spectroscopic investigations of Ca in liquid helium [105]. After comparing with some other atomic impurities, Ca, on the other hand, has been suggested as the ideal dopant to detect vortices in helium clusters [106].

3.1. Calculation Details

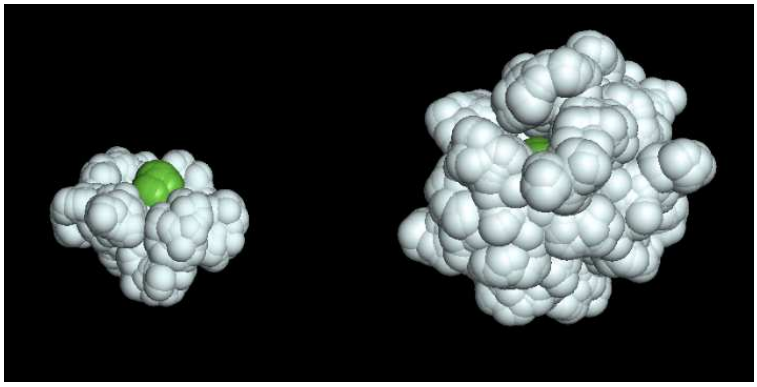

Figure 2. Snapshot taken from the PIMC simulation for He_NCa, with $N = 10$ (left) and $N = 40$ (right) at $T = 1$ K using the He-Ca P1 potential from Ref. [94]. Beads for the dopant are in green whereas white is for He atoms.

The PIMC calculations [107] at temperatures between 1 and 2 K have been performed by means of the energy estimator from Eq. (7). Spheres centered at the Ca atom with a radius of 30 Å and at the CM of the He droplet with a radius of 15 Å have been defined to restrict the movements of the He atoms in order to avoid

their possible evaporation from the cluster. These values of the radii are relaxed to 24 and 12 Å in the case of $T = 1$ K. The simulations were carried out using the He–He potential by Aziz and Slaman [93] and two possible He–Ca interactions: (i) the potential reported by Kleinekathöfer [94] (hereafter denoted as P1) and (ii) the potential reported by Lovallo and Klobukowski [95] (hereafter denoted as P2). These dopant–He potentials differ both in the analytical form and in their intrisic properties. The P1 potential for example corresponds to the Tang-Toennies model [108] fitted according to the numerical expression:

$$V(r) = D\exp(-b_1 r - b_2 r^2) + V_{\rm disp}(r), \tag{15}$$

with $D = 3.19\,E_h$, $b_1 = 1.05\ \mathrm{a}_0^{-1}$, $b_2 = 0.00745\ \mathrm{a}_0^{-2}$ and in which the long-range term $V_{\rm disp}$ is described by the dispersion series:

$$V_{\rm disp}(r) = -\sum_{n\geq 3}^{5} f_{2n}(b'(r), r)\frac{C_{2n}}{r^{2n}}, \tag{16}$$

where the corresponding coefficients, $C_6 = 46.8\,E_h\ \mathrm{a}_0^6$, $C_8 = 1835\,E_h\ \mathrm{a}_0^8$ and $C_{10} = 118500\,E_h\ \mathrm{a}_0^{10}$ are taken from Ref. [109], and the damping functions $f_{2n}(b'(r), r)$ are calculated as:

$$f_{2n}(b'(r), r) = 1 - e^{-rb'(r)}\sum_{k=0}^{2n}\frac{(rb'(r))^k}{k!}, \tag{17}$$

with $b'(r) = b_1 + 2b_2 r$, as defined in Refs. [94, 110].

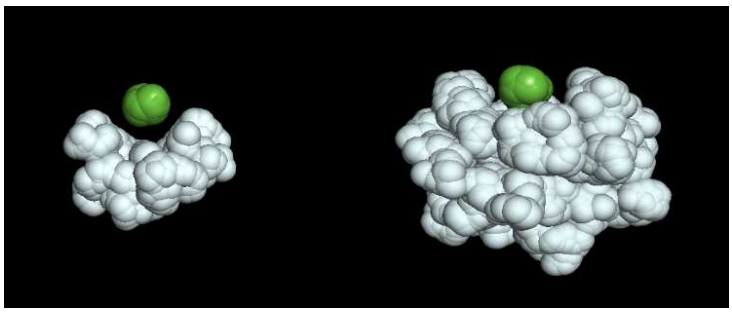

Figure 3. Same as Fig. 2 for the PIMC calculation performed with the P2 He-Ca potential from Ref. [95].

The P2 potential [95] however is obtained by means of the *ab initio* well-tempered model core potential method. Lovallo and Klobukowski [95] used coupled-cluster level of theory with single and double excitations and a perturbational treatment of the triple excitations in the series of pair potentials between He and Group 2 elements. Present calculations were performed employing the numerical fit to *ab initio* points between 2 Å and 16.0 Å of Ref. [100] according to the expression:

$$V(r) = Ae^{-kr}/r \qquad r \leq r_0$$
$$= \sum_{n=3}^{7} c_{2n}/r^{2n} \quad r \geq r_0 \tag{18}$$

where r_0 = 4.6 Å, A = 2040362.862 cm^{-1} Å, k = 2.088 Å^{-1}, c_6 = 231619.170 cm^{-1} Å^6 , c_8 = 15438995.509 cm^{-1} Å^8 , c_{10} = 2085441484.937 cm^{-1} Å^{10} , c_{12} = 82383199752.866 cm^{-1} Å^{12} and c_{14} = 852545635932.049 cm^{-1} Å^{14}.

Differences between He–Ca P1 and P2 potentials regarding both well depth and minimum energy distances are manifested in the Figure 1 with all the interparticle interactions employed in the calculations of Ref. [107]. Thus, the P1 potential is clearly deeper than the P2 one ($\sim$ 10 cm^{-1} in comparison with $\sim$ 3.5 cm^{-1}, respectively) and predicts a shorter distance between the He and Ca atoms at the equilibrium ($\sim$ 7 Å versus $\sim$ 8 Å respectively). In addition the He–He interaction is clearly deeper than the P2 potential but shallower than the P1 He–Ca interaction. These noticeably different characteristics between the interparticle potentials under consideration are expected to yield distinct properties for the He$_N$-Ca clusters.

3.2. Results

The energies for the He$_N$Ca clusters with N = 10, 20, 30 and 40 at T = 1, 1.5 and 2 K obtained by means of the PIMC approach are shown in Table 1. For each size, the energies are found to be less negative as the temperature increases, whereas at a constant value of T the addition of more He atoms makes the cluster more stable. Remarkably, for the less deep P2 potential, positive energies have been obtained for high temperatures and small clusters. The analysis of the possible stability of the systems under study has been also completed by comparing with the energies of the corresponding pure He$_N$ clusters. Boronat *et al* [111] reported PIMC results at certain values of temperature which indicate that: (i) He$_{20}$ displays positive energy for $T \geq$ 1.5 K and (ii) He$_{40}$ has an energy of -34.08 $\pm$ 3.59 cm^{-1} at T = 1.5 K. It is therefore possible to conclude that the PIMC calculations using the P1 potential predict stable He$_N$Ca clusters for the sizes and temperature range under study. The situation with the P2 potential is on the contrary more subtle and the stable existence of He$_{40}$Ca at T = 1.5 K, for example, is subject to the uncertainties of the error bar of the PIMC calculation for the pure He clusters and the use of different He–He interactions (the potential employed in the calculation of Ref. [111] corresponds to an alternative version of the potential by Aziz and collaborators reported in Ref. [112]).

In addition, the sequence of energies as a function of T was found to correlate reasonably well following the extrapolation law $a_1 + a_2 e^{T/a_3}$ to results obtained at T = 0 K by means of diffusion MC (DMC) calculations [107]: -44.80 and -12.25 cm^{-1} for the P1 and P2 He–Ca potentials, respectively, for He$_{10}$Ca, and -96.23 cm^{-1} and -33.65 cm^{-1} for He$_{20}$Ca.

A clear manifestation of the different structure of the clusters according to the intrisic nature of the dopant-impurity interaction is observed by means of the PIMC

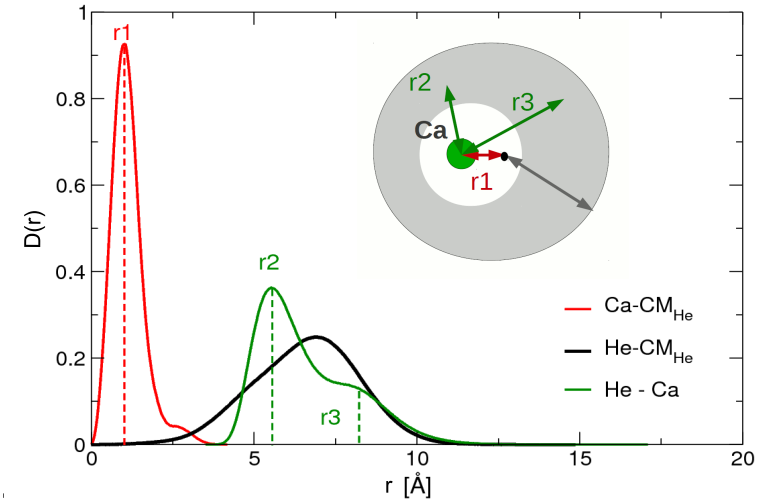

Figure 4. Probability density functions of the internal distances (Ca–CM_{He} in red, He–CM_{He} in black and He–Ca in green) in $He_{40}Ca$ clusters obtained with the PIMC method at $T = 1$ K with the P1 He-Ca potential. A graphical scheme of the doped cluster configuration is included.

Table 1. PIMC energies for the $He_N Ca$ clusters with $N = 10, 20, 30$ and 40 obtained with the P1 (from second to fith columns on the left side) and P2 (from sixth to ninth columns on the right side) He–Ca potentials at $T = 1$ K. Units are cm^{-1}.

T (K)	$N = 10$	$N = 20$	$N = 30$	$N = 40$	$N = 10$	$N = 20$	$N = 30$	$N = 40$
1	-38.60	-86.71	-118.97	-137.16	-2.67	-14.51	-30.21	-56.93
1.5	-32.12	-72.08	-109.75	-128.28	–	–	-11.74	-31.76
2	-24.65	-52.79	-71.85	-113.50	–	–	–	-3.52

simulations. In particular snapshots for $He_{10}Ca$ (left) and $He_{40}Ca$ (right) using the P1 potential at $T = 1$ K shown in Figure 2 indicate that the impurity gets partially solvated as He atoms are added to the cluster.

However the same number of He atoms is not capable to surround the dopant when the P2 potential is employed. As shown in Figure 3 the Ca atom occupies a dimple formed by the helium droplet for $He_{40}Ca$ (right) which in fact is already created at $N = 10$ (left). The apparent weakness of the He–Ca interaction yields a location of the impurity on the surface of the helium cloud, a configuration which, in case to remain for even larger sizes, would be compatible with experimental observations [24, 60, 103].

A schematic insight of the different geometries depending on the He-Ca potential is also gained by means of the probability density functions on the pairwise distances within the clusters. Peaks in the distributions on the different internal distances shown in Figure 4 for the calculation with the P1 potential for $He_{40}Ca$ at $T = 1$ K

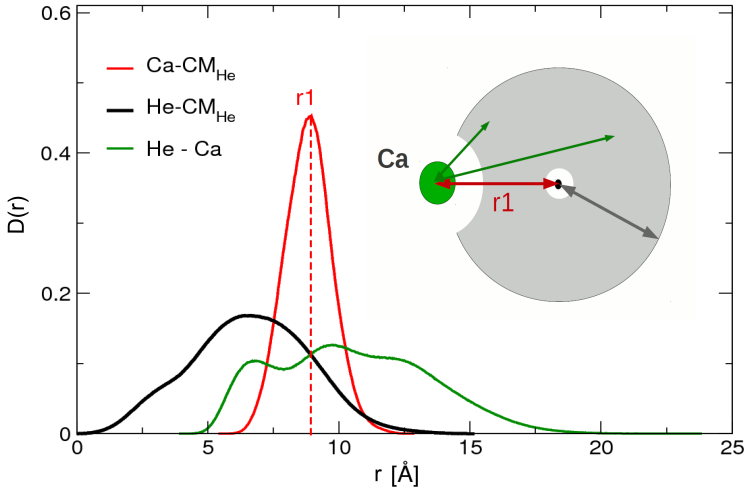

Figure 5. Same as Figure 4 for the P2 He-Ca potential.

can be interpreted in consistence with a partial solvation. Thus, the narrow maximum for the distance between Ca and the helium droplet CM (red line) at short values ($\sim$ 1.5 Å) corresponds to the impurity embedded into an almost spherical bubble; peaks of the bimodal structure seen for the He-Ca distributions (green line) correlates with distances to the internal cavity around the Ca atom and the outer surface of the helium droplet, and finally the broad asymmetric distribution for the distances between He atoms and its CM suggests a sufficiently extended helium droplet to possibly cover the impurity.

A similar analysis performed for the probability densities obtained with the P2 potential reveals on the contrary a geometry in which, as discussed before, the Ca sites outside the He droplet. Thus: (i) the preference for a long separation ($\sim$ 9 Å) between the Ca atom and the CM of the He cloud observed in Figure 5, is only possible if the dopant remain outside the droplet, and (ii) the more diffused bimodal structure of the distribution along the Ca–He distance in comparison to results obtained with the P1 potential discards the location of the impurity inside the droplet closed to the CM of the helium atoms.

4. He_N-Rb_2

High-spin alkali dimers have a larger survival probability within helium droplets than the singlet-states which release more energy after excitation with the subsequent detachment of the molecule from the cluster [113]. This feature explains why most of the Helium Nanodroplet Isolation (HENDI) [114] spectroscopic experiments have been performed on triplet-state alkali diatoms [115]. In particular, ground triplet-state

Rb_2 attached to helium clusters has been the subject of numerous theoretical [30, 31, 116] and experimental investigations [117–123]. The dynamics of vibrational wave packets in triplet states of Rb_2 formed on helium nanodroplets was systematically investigated using femtosecond pump-probed photoionization spectroscopy [120]. The $(2)^3\Pi_g \leftarrow a\,^3\Sigma_u^+$ band of Rb_2, which gets finally detached from the helium cluster upon electronic excitation, was analyzed. Transitions between low-lying triplet states and singlet states were identified. This work was subsenquently completed with the analysis of the obtained spectra by means of empirically determined effective coupling spin-orbit Hamiltonian for the corresponding potential energy curves [119, 124].

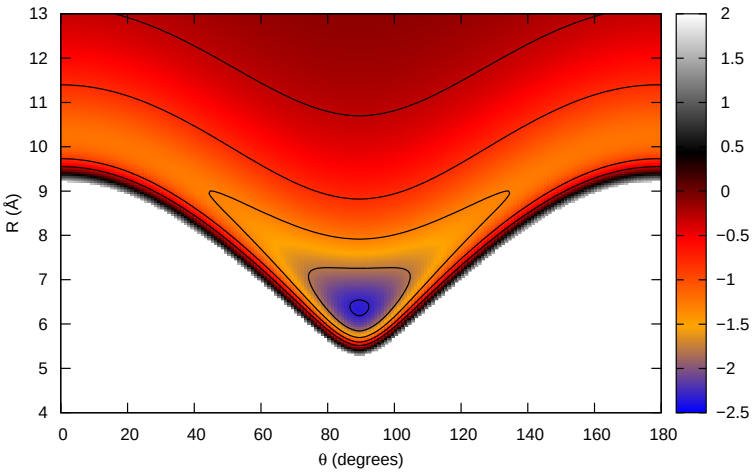

Figure 6. Potential energy for the He–Rb_2 interaction from Ref. [116].

DMC and PIMC calculations have been performed on recently published PES for the He–$Rb_2(^3\Sigma_u^+)$ system [30, 116, 125]. Authors of Ref. [116] found that the internal vibrational degree of freedom of Rb_2 could be neglected and reported a structural transition from He_2-Rb_2 to He_3-Rb_2 and He_4-Rb_2. In particular, the two He atoms of the first case were located at both sides of the diatomic dopant, being the system with $N = 3$ an intermediate configuration with respect to He_4-Rb_2 in which the rare gas diatom behaves as an independent subcomplex of the He cloud. In an attempt to investigate possible previous steps in the formation of Rb_2 doped He clusters, inelastic and reactive scattering processes between Rb and He atoms have been subject of study at low temperatures [125–127].

4.1. Calculation Details

PIMC calculations were performed for He_NRb_2 clusters, with N between 10 and 40 at $T = 1$ and 2 K assuming the Rb_2 as a linear rigid rotor [82] with an interparticle

Table 2. Parameters for the analytical fitting to the *ab initio* results of Ref. [116] for the interaction potential between the He atoms and Rb_2, defined in Eqs. (20)-(22). Units of $d(0)$ and $d(\pi/2)$ are cm^{-1} and for $\bar{x}(0)$ and $\bar{x}(\pi/2)$ are Å.

α_1	α_2	$d(0)$	$d(\pi/2)$	$\bar{x}(0)$	$\bar{x}(\pi/2)$
15.214	6.173	0.7987	1.1730	7.6044	7.096

distance between the Rb atoms of 6.35 Å. The simulations were performed under constraints for the movements of the He atoms in order to avoid their evaporation. In particular they are confined inside a sphere of radius 30 Å centered at the CM of Rb_2 and can not exceed a maximum distance of 15 Å away from the CM of the helium droplet. For the rotational analysis a value of 9.8×10^{-3} cm^{-1} [82, 116] was taken for the Rb_2 rotational constant B in Eq. (8).

The He–He interaction was described according to the Aziz and Slaman potential [93], whereas for the interaction between the He atom and Rb_2 the analytical fit of *ab initio* points as reported in Ref. [116] was employed. Such a potential, shown in Figure 6, corresponds in essence to the sum of two angle-dependent Lennard-Jones interactions as:

$$W(r_{\rm eq}, R, \theta) = V(R_1, \theta) + V(R_2, \theta) \tag{19}$$

where R_i is the distance between He and the i-th Rb atom, and each potential can be expressed as

Figure 7. Initial configuration for the $He_{20}Rb_2$ cluster via the EA approach.

$$V(x, \theta) = d(\theta) \left[\left(\frac{\bar{x}(\theta)}{x} \right)^{12} - 2 \left(\frac{\bar{x}(\theta)}{x} \right)^{6} \right] \tag{20}$$

with $d(\theta)$ and $\bar{x}(\theta)$ being the well depth and equilibrium distance at a fixed value of the orientation θ. Assuming a dependence for such coefficients on the angle θ as:

$$d(\theta) = d(0) + [d(\pi/2) - d(0)]\, sin^{2\alpha_1}(\theta) \tag{21}$$

$$\bar{x}(\theta) = \bar{x}(0) + [\bar{x}(\pi/2) - \bar{x}(0)]\, sin^{2\alpha_2}(\theta) \tag{22}$$

and by means of fittings to the *ab initio* points for the linear and perpendicular geometries, the values for the corresponding parameters shown in Table 2 are obtained.

The minimum of the PES shown in Figure 6 is located close to $\theta \sim 90°$, thus suggesting that the equilibrium geometry of the Rb_2-doped helium clusters should correspond to a T-shape arrangement. In fact, that is exactly what an EA optimization calculations predicts. According to this classical approach, the low energy configuration for the cluster with $N = 20$ He atoms, shown in Figure 7 has the helium clusters localized away from the diatomic dopant around the perpendicular direction with respect ot the Rb–Rb molecular axis. EA estimates yield values of -582.66 cm^{-1} for $He_{20}Rb_2$ and -1321.06 cm^{-1} for $He_{40}Rb_2$ for the lowest classical potential energy levels. As dicussed in the Introduction section, these optimised configurations, after refinements performed with the CMC to account for thermal effects, are taken as the initial geometries for the PIMC simulations.

4.2. Results

The rotation and translation of the molecular species introduces variations in the energies of the droplets in comparison with the values obtained when the mass of the Rb_2 has been considered large enough to neglect its kinetic contribution [116]. PIMC calculations under the assumption that the diatomic dopant is free to move and rotate, as explained in Eqs. (8)-(10), yield less negative energies. Thus, for the case of $He_{20}Rb_2$ at $T = 1$ K, a value of $E_{\mathrm{rot-tra}} = -10.32$ cm^{-1} is obtained in comparison with $E_{\mathrm{fix}} = -15.08$ cm^{-1}. This difference of about ~ 5 cm^{-1} between both energies becomes larger when either the temperature or the number of He atoms is increased. For example, for $N = 40$ the PIMC energies at the same temperature are $E_{\mathrm{rot-tra}} = -50.52$ cm^{-1} and $E_{\mathrm{fix}} = -62.86$ cm^{-1}, whereas at $T = 2$ K, these values become -0.37 and -15.54 cm^{-1}, respectively. This kind of comparison has been also previously established for systems such as He_N-OCS [128]. The analysis of the rotational dynamics of the Rb_2 on a helium surface [30] reveals that the in-plane rotation is weakly perturbated by the environment whereas the out-plane contribution is hindered with the only possibility of a pendular movement. In this sense, the presently reviewed PIMC investigation for helium droplets [82] concluded that at $T = 1$ K, the total rotational energy, 1.2 cm^{-1}, for both He_{20}-Rb_2 and He_{40}-Rb_2 is the result of 0.7 cm^{-1} in-plane rotation and 0.5 cm^{-1} of out-plane rotation. However, as the temperature increases up to $T = 2$ K, most of the rotation is due to the in-plane contribution thus suggesting a negligible effect coming from the helium environment.

The effect of including the rotational degree of freedom of the dopant can be also analyzed through the corresponding probability density functions. In particular Figure 8 shows radial distributions of $He_{20}Rb_2$ at $T = 1$ K obtained by means of PIMC calculations for a fixed (left panel) and a rotating Rb_2 (right panel). The results

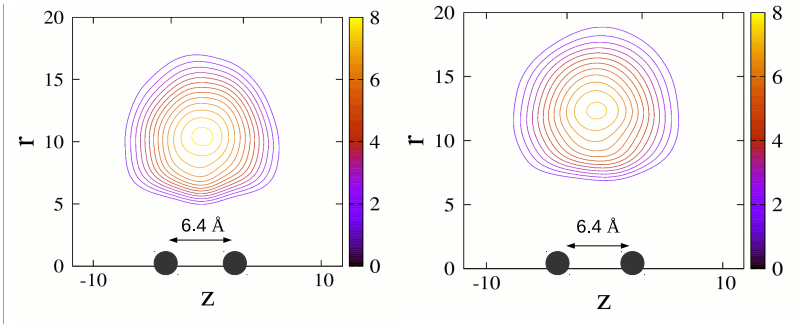

Figure 8. Probability density function for He_{20}-Rb_2 at $T = 1$ K obtained by means of the PIMC approach with a fixed dopant (left) and rotating Rb_2 (right). Rb atoms are included as spheres separated a ~ 6.4 Å equilibrium interparticle distance. Distances are measured in Å and values of the distribution has to be multiplied by 10^{-3}.

indicate that the distance of the He droplet with respect to the dopant, represented at the bottom of the figure with the two Rb atoms separated about 6.4 Å increases when the diatomic impurity is free to rotate. In addition the helium atoms seem to occupy a more delocalised region, thus suggesting that they actually feel the internal excitation of the Rb_2 moiety in spite of the existing separation.

Energies for the doped clusters with a fixed and rotationless Rb_2 impurity are shown in Fig. 9 for $N = 20$ and 40 as a function of the temperature. As expected the clusters become less stable as the temperature increases but the addition of He atoms results in stability for the whole system. The stability of the doped clusters however is usually tested by direct comparison with the corresponding energies for the pure He_N systems. Figure 9 shows energies for both He_NRb_2 and He_N, with $N = 20$ and 40, at temperatures between $T = 1$ and 2 K. From the dependence with the temperature observed in the figure, it is clear that the smallest cluster is not stable beyond 1.5 K, and the addition of the Rb_2 does not improve the situation. Energies for doped and pure clusters are very close in this system, thus suggesting that for a small number of He atoms, the former is hardly bound. The situation seems to be more favourable for stable bound states for the $He_{40}Rb_2$ system. Values of the energy as T increases remain sufficiently below the corresponding energies for the pure He_{40} cluster to guarantee the stability of the doped clusters. In fact, at $T = 2$ K the impurity is capable to make the whole system bound, something that does not happen in the absence of Rb_2.

Precise information regarding the structure of the clusters is obtained by analysis

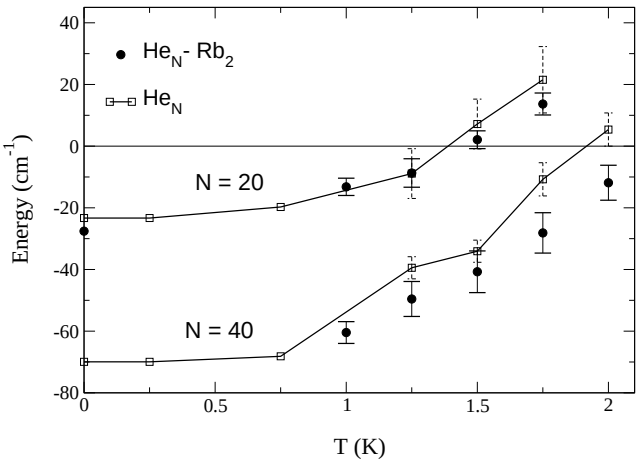

Figure 9. PIMC energies of the He_N-Rb_2 clusters for $N = 20$ and 40 (in solid circles) calculated at a temperature range between 1 and 2 K assuming a fixed and rotationless impurity. Results for pure He_N clusters (in empty circles) from Ref. [111] are included for comparison. DMC result from Ref. [31] for $He_{20}Rb_2$ is also shown to see the trend with T.

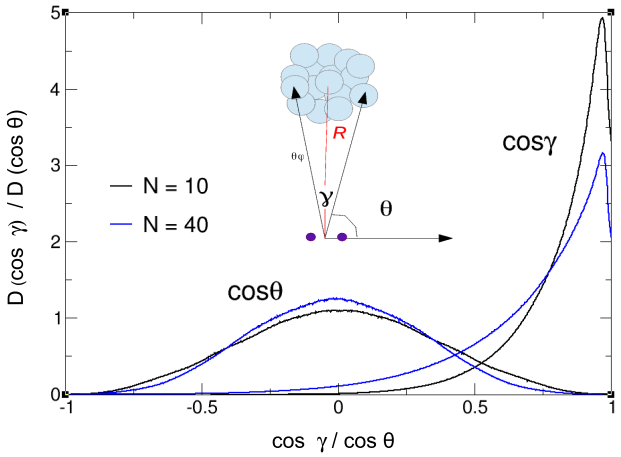

Figure 10. Angular distributions as a function of $\cos\theta$ and $\cos\gamma$ obtained by means of the PIMC approach for He_NRb_2 with $N = 10$ and 40 at $T = 1$ K. A graphical scheme to interpret the geometry of the two clusters is included. See text for details.

of the corresponding probability density functions. In particular, Figure 10 shows the angular distributions for the $N = 10$ and $N = 40$ cases. As indicated in the schematic diagram included in the figure, peaks around $\cos\gamma \sim 1$ in combination with the observed distribution on $\cos\theta$, suggests the formation of a compact helium aggregate at a T-shaped configuration with respect to the Rb_2 diatom axis. The slight variations on the value of the angle as more He atoms are added to the clusters, as

manifested by the comparison between the $He_{10}Rb_2$ and $He_{40}Rb_2$ systems in Figure 10, simply correspond to the larger volume occupied by the cluster as its size increases.

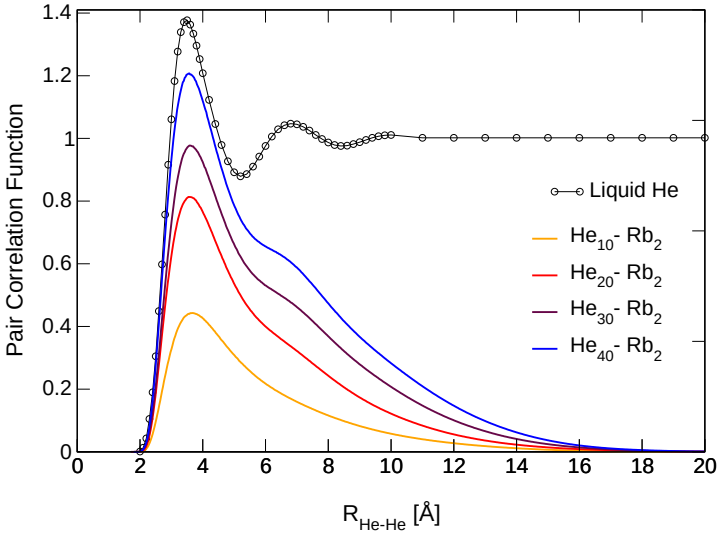

Figure 11. Pair correlation function obtained for different sizes of the He_N-Rb_2 system ($N = 10, 20, 30$ and 40). The result for the liquid helium reported in Ref. [129] is also included for comparison.

A remarkable effect observed when more He atoms are added can be seen in Figure 11 where the pair correlation functions for He_NRb_2, with N from 10 to 40 is compared with the result found for the pure bulk helium at $T = 1$ K [129]. Such a comparison reveals that part of the structure of the experimental function can be reproduced as N increases. If the main peak at $R_{\mathrm{He-He}} \sim 4.9$ Å is already found even for the lowest cluster, $He_{10}Rb_2$, the addition of He yields to a much more defined peak and the development of a secondary maximum of the simulated distribution around ~ 7 Å resembling the experimental data. A similar comparison between MC results for small doped clusters and experimental pair distributions was also established for He_NCs_2 [130]. The equilibrium geometry which leaves Rb_2 outside the He droplet favours that some features associated to pure helium could be at least suggested in the doped cluster. The remarkable thing, in addition, is to find indications of this typically liquid behaviour in finite size droplets with less than hundred He atoms.

5. He_N-He^{*-}

Atomic He anions, besides free electrons, play a fundamental role as charge carriers in a superfluid-like environment. Insights regarding the formation of such ions were inferred via crossed beam scattering experiments with supercritical liquid free jet expansions [131]. Preliminary theories suggesting the direct interaction of electrons with neutral He droplets as the main source to produce these ionic species were soon substituted by a process mediated by electronic excitation to metastable states [131–133]. In fact the most likely production mechanism consists of two steps:

$$\mathrm{He}(1s^2\,{}^1S) + e^-(22\,\mathrm{eV}) \rightarrow \mathrm{He}^* \tag{23}$$

$$\mathrm{He}^* + e^-(0\,\mathrm{eV}) \rightarrow \mathrm{He}^{*-} \tag{24}$$

where He^* is $\mathrm{He}(1s2s\,{}^3P)$, the first excited state of He, formed with an incident electron with sufficient kinetic energy to account for both the required penetration energy (1.2 eV) [134] and the excitation energy of 19.8 eV from the ground state. The atomic He anion, He^{*-}, is formed after the encounter of the separate bubbles within the He clusters which contain the resulting zero kinetic energy electron and He^* as written in Eq. (24) [132, 135–137]. The first detection of He^{*-} as a fast ion in bulk helium was reported in Refs. [138, 139].

5.1. Calculation Details

The PIMC calculations [140] were performed at $T = 0.4$ K using the thermodynamic energy estimator given by Eq. (6). The sampling procedure for the multislice many-particle movements is the multilevel Metropolis method [61, 63, 90], with $M = 8$ beads involved in each MC step. Up to a total of 4 He atoms are allowed to take part in the exchange permutation sampling employed to include the bosonic symmetry; a value tested for both pure and doped helium clusters [63, 141]. Given the low temperature considered in the PIMC calculations, large thermal excitation is not expected so no confining limitation to the movement of the He atoms was imposed.

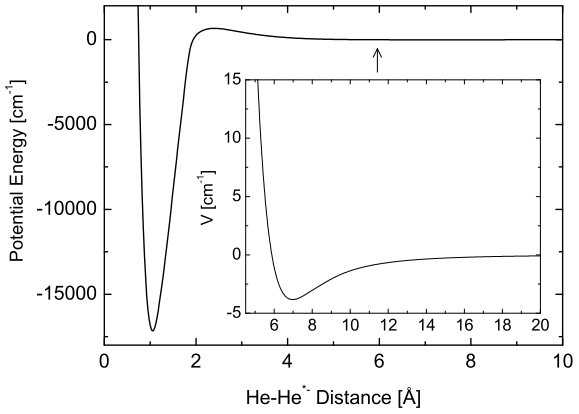

Figure 12. Potential energy function for the He–He^{*-} interaction according with the analytical fit of Eq. (25) to the *ab initio* points of Ref. [135]. The inset shows the region of the secondary minimum amplified.

The He–He interaction has been described by means of the potential reported by Aziz and Slaman [93] and for the potential between the atomic ion He^{*-} and the

Table 3. Parameters for the interaction potential $V_{\text{He-He}^{*-}}(r)$ between the He atoms and He^{*-} (See Eqs. (25)-(30)).

	$j=0$	$j=1$	$j=2$	$j=3$	$j=4$
D_j (cm^{-1})		17,109.4319	668.0	3.82	
α_j ($\mathring{A}^{-1}$)		2.2202	2.1612	0.6330	
$\tilde{\alpha}_j$ ($\mathring{A}^{-1}$)		2.2202	1.4313	0.6330	
$\bar{r}_j$ ($\mathring{A}$)		1.06	2.40	6.97	
a_j (cm^{-1})	22,367.3596	1	1	1	1
b_j (cm^{-1})	20,533.7740	0	0	0	0
β_j ($\mathring{A}^{-1}$)	2.1751	11.1642	9.6603	1.7588	2.0478
$\bar{x}_j$ ($\mathring{A}$)	1.4816	1.1312	1.8168	4.1645	8.2767

He atoms a numerical fit to the *ab initio* points calculated by Huber and Mauracher [135] has been performed according to the following expression:

$$V_{\text{He-He}^{*-}}(r) = [1 - g_4(r)]\,\mathcal{F}_{\text{III}}(r) + \frac{c_4 g_4(r)}{r^4} \tag{25}$$

where $c_4 = -13,683.2521$ $\mathring{A}^{-4}$ cm^{-1} and

$$\mathcal{F}_{\text{III}}(r) = \mathcal{F}_{\text{II}}(r)\,[1 - g_3(r)] + g_3(r) f_3(r), \tag{26}$$

where

$$\mathcal{F}_{\text{II}}(r) = [1 - g_2(r)]\,\mathcal{F}_{\text{I}}(r) - g_2(r) f_2(r), \tag{27}$$

with

$$\mathcal{F}_{\text{I}}(r) = [1 - g_1(r)]\,f_1(r) + g_1(r) g_0(r). \tag{28}$$

In the above Equations (25)-(28), we have defined:

$$f_j(r) = D_j e^{-\tilde{\alpha}_j (r - \bar{r}_j)} \left(e^{-\alpha_j (r - \bar{r}_j)} - 2 \right) \tag{29}$$

$$g_j(r) = \frac{a_j}{2} \left(1 + tanh\left[\beta_j (r - \bar{x}_j)\right]\right) - b_j \tag{30}$$

with values for the corresponding parameters given in Table 3.

The potential, shown in Figure 12, exhibits a well of about $\sim 17,000$ cm^{-1} deep with the minimum located at $r = 1.06$ $\mathring{A}$(region I). The numerical fit also includes the description of a barrier around ~ 2.2 $\mathring{A}$, (region II), which leads to a much narrower minimum (~ 3.8 cm^{-1}) (region III) than the one in region I. This well, located at $r \sim 7$ $\mathring{A}$, similar to some other He-impurity potentials, preceeds to the asymptotic regime (region IV).

5.2. Results

The preliminar inspection of the equilibrium configurations for the different He_N-He^{*-} clusters by means of the EA reveals that the impurity is surrounded by the He atoms as N increases which form a bypiramid of six atoms around it.

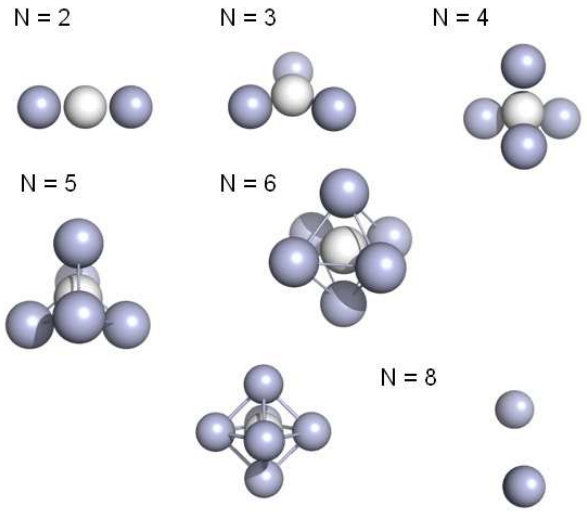

Figure 13. Geometries of the He_N-He^{*-} clusters for $N = 2 - 6$ and 8 obtained by means of the EA.

As shown in Figure 13, additional atoms are located at further distances away from this central structure. The corresponding energies for these droplets also manifest the formation of this specific core, with larger contributions to the total energy coming from the atoms in the bypiramid. Table 4 presents EA predictions for the potential minima in comparison with the PIMC and CMC results at $T = 0.4$ K. A similar trend is observed for $E_{\rm PIMC}$, $E_{\rm CMC}$ and $E_{\rm EA}$ with noticeable differences between the energies for consecutive He_{N-1}-He^{*-} and He_N-He^{*-} clusters when the He atoms occupy the position associated with the deep He-impurity potential minimum up to $N = 6$. Beyond this point a sudden stabilization occurs as the size of the system increases. Once the bypiramid is formed the only accessible minima for the remaining helium atoms are those corresponding to the narrower well around $r_{\rm He-X} \sim 7$ Å and the existing one for the He–He interaction at $r_{\rm He-He} \sim 2.97$ Å.

The comparison in Table 4 of the EA and CMC energies reveals the role played by possible thermal effects on the system. Given the good agreement between both sets of results one may conclude that the temperature considered in the present study, $T = 0.4$ K, is certainly not large enough to introduce significant thermal excitation into the system. $E_{\rm EA}$ remains in general below the $E_{\rm CMC}$ values, but the uncertainties on the accuracy of the EA to explore equilibrium configurations when the deep potential well has been already occupied and the shallow secondary He–He^{*-} potential minimum is the only stable option for the He atoms, may question the actual predictions of the method. Differences with respect to the PIMC energies on the other hand can be attributed mainly to QM effects. Values of $E_{\rm PIMC}$ for $N \gtrsim 8$ seem to be somehow affected by the He–He interaction: thus, despite the actual error bars, the energy for the He_8-He^{*-} cluster could be in principle understood as the combination of the bipyramid structure He_6He^{*-} plus an external He_2 unit with the energy of the He–He equilibrium distance.

Table 4. Energies of the He_N-He^{*-} systems obtained by means of the PIMC (second column), the CMC (third column) and the EA (fourth column) approaches. Units are cm^{-1} and errors for the PIMC results are in parentheses.

N	PIMC	CMC	EA
1	-17,013.8 (28.0)	-17,169.0	-17,169.1
2	-33,707.0 (46.5)	-34,133.7	-34,134.6
3	-48,588.0 (126.1)	-49,207.8	-49,208.6
4	-61,342.0 (98.5)	-61,925.8	-61,927.1
5	-66,412.4 (268.3)	-67,685.0	-67,686.7
6	-72,378.7 (262.2)	-74,001.6	-74,003.8
7	-72,392.4 (267.6)	-74,005.9	-74,008.1
8	-72,385.5 (186.7)	-74,017.8	-74,012.0
16	-72,613.6 (206.0)	-74,246.7	-74,252.3
32	-72,988.5 (224.6)	-74,660.8	-74,601.3

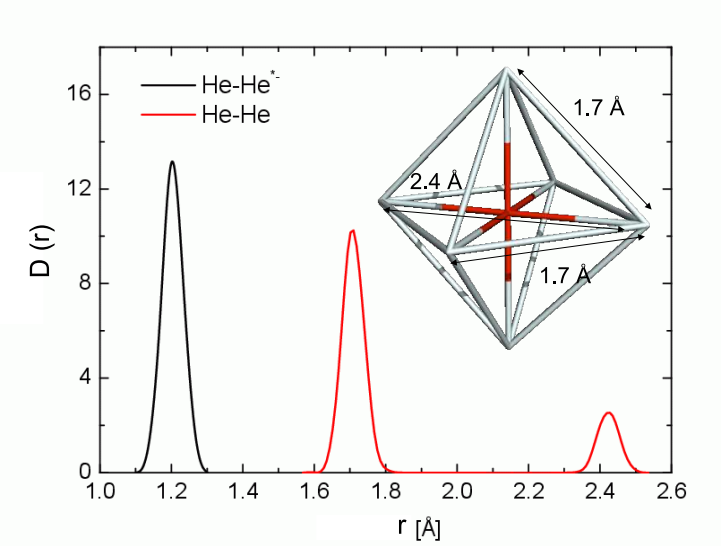

Figure 14. PIMC probability densities for the He–He^{*-} (black) and He–He (red) distances for the He_6-He^{*-} system at $T = 0.4$ K according to Eqs. (11) and (12). The bipyramid structure with the corresponding interparticle distances is included as inset.

The central structure formed by the impurity at the center of a bipyramid solvated by six He atoms can be characterized by means of the PIMC density probabilities for both the He–He and He–He^{*-} distances, shown in Figure 14. Maximum peaks of the densities can be correlated with the interparticle distances in the equilibrium configuration predicted by the EA: thus the maximum at $r_{\mathrm{He-He^{*-}}} \sim 1.2$ Å for $D_{\mathrm{X}}^{(6)}(r)$ corresponds to the distances between the dopant and the He atoms of the vertices of the bipyramid, whereas for the $D_{\mathrm{He}}^{(6)}(r)$ distribution, the main maximum

at $r_{\mathrm{He-He}} \sim 1.7$ Å describes the distance between He atoms placed in the central structure. The secondary maximum at $r_{\mathrm{He-He^{*-}}} \sim 2.4$ Å describe the two pairs of opposed He atoms with the impurity in between in the square basis of the bipyramid.

The presence of this central rigid structure for larger clusters is manifested in the comparative analysis of the angular distributions. Figure 15 shows the γ density probabilities for the $N = 6$ and $N = 32$ cases. $D_\gamma^{(6)}$ exhibits two clear peaks at $\cos\gamma \sim 0$ and $\cos\gamma \sim -1$, corresponding to the two only possible angles formed by two He position vectors in the bipyramid: respectively, 90° for pairs of consecutive helium atoms and 180° for those separated by the He^{*-} impurity. This angular pattern remains in the distribution for $D_\gamma^{(32)}$ (see Figure 15) which displays clear signatures of these two peaks besides a broad increasing background probability as $\cos\gamma$ changes from -1 to 1, which comes from the rest of He atoms.

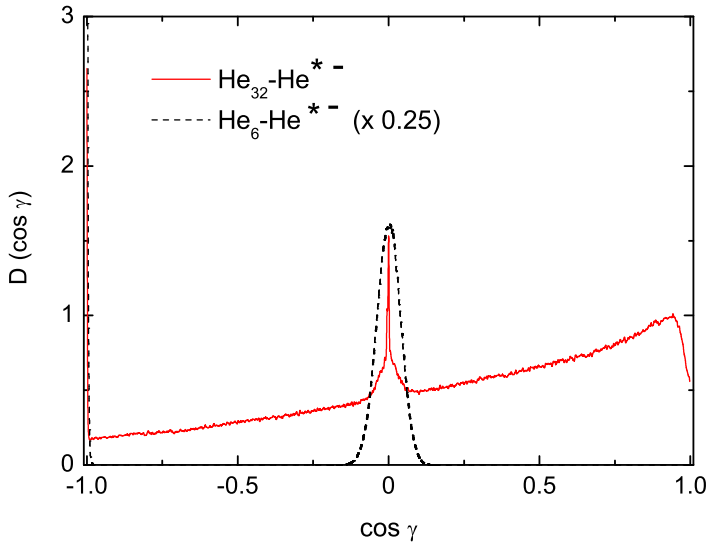

Figure 15. PIMC angular probability density distributions for $\cos\gamma$ (see Eq. (13) for details) for the He_6-He^{*-} (black dashed line) and He_{32}-He^{*-} (red solid line) clusters at $T = 0.4$ K. The distribution for the $N = 32$ case is multiplied by a factor 1/4 for the sake of comparison.

According to Ref. [135], the potential minimum of the He^{*-}-He system has the structure of a He_2^+ core besides a diffuse electronic shell due to the two electrons occupying σ and π orbitals. Thus, the inner solvating cage seems to be formed by an ensemble of He^+ cations which share an electronic cloud. This "chemical bound" configuration found for short distances becomes however a "polarisation-bound" structure as the distance increases beyond the potential barrier exhibited by the He^{*-}-He potential around ~ 2.5 Å. Additional He atoms feel a much weaker potential due to the screening induced by the presence of the inner core of six atoms surrounding the

impurity and move further out to the shallower secondary potential minimum located at $\sim 7 - 8$ Å.

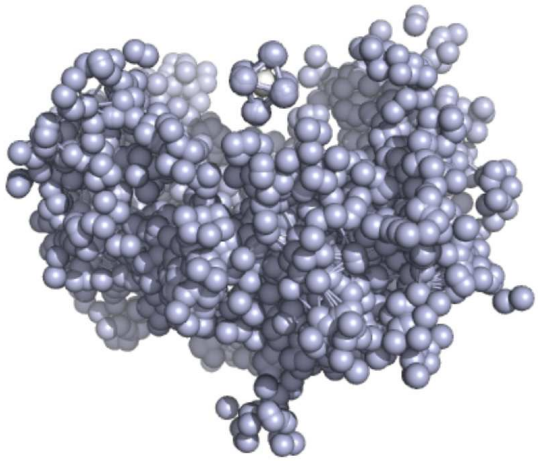

Figure 16. Snapshot from the PIMC simulation for He_{32}-He^{*-} at $T = 0.4$ K. The bipyramid structure can be seen in a dimple at the top.

The stable and rigid helium structure of inner He atoms around the atomic anion could be interpreted as consistent with the previously suggested heliophilic character for He^{*-} [132]. However, the dopant inside the central cage is not completely solvated but placed inside a broad dimple. The snapshot in Figure 16 corresponds to the PIMC simulation for the cluster with $N = 32$ at $T = 0.4$ K with $M = 100$ beads and shows how the remaining twenty-six atoms leave the He^{*-} unit unconvered. One explanation for the distance between the solvating He atoms and those fixed in the central structure can be found in the competition of the He–He and He–Impurity interactions. According to the first one, the separation between these two types of helium atoms should be, as in the bipyramid, ~ 2.9 Å, the equilibrium distance for such an interaction. However that would mean the outer atoms to locate ~ 4.5 Å away from the He^{*-} dopant, somehting, in principle, forbidden by the presence of the barrier separating both the deep inner well and the shallow one at larger distances. Whether or not the addition of a noticeably larger number of He atoms would yield the formation of bubble structures surrounding the He_6-He^{*-} core remains an open question.

Differences between the environment felt by the He atoms depending on their precise location inside the droplet are manifested by the analysis of permutation paths when the exchange symmetry is properly taken into account in Equation (3). Those atoms in the vertices of the bipyramid are expected to display a rigid localization with almost no freedom to move and the corresponding path in the PIMC simulation looks in essence like one corresponding to an unique bead. External He atoms on the contrary will be more delocalized and could take part in exchange PIMC paths. This

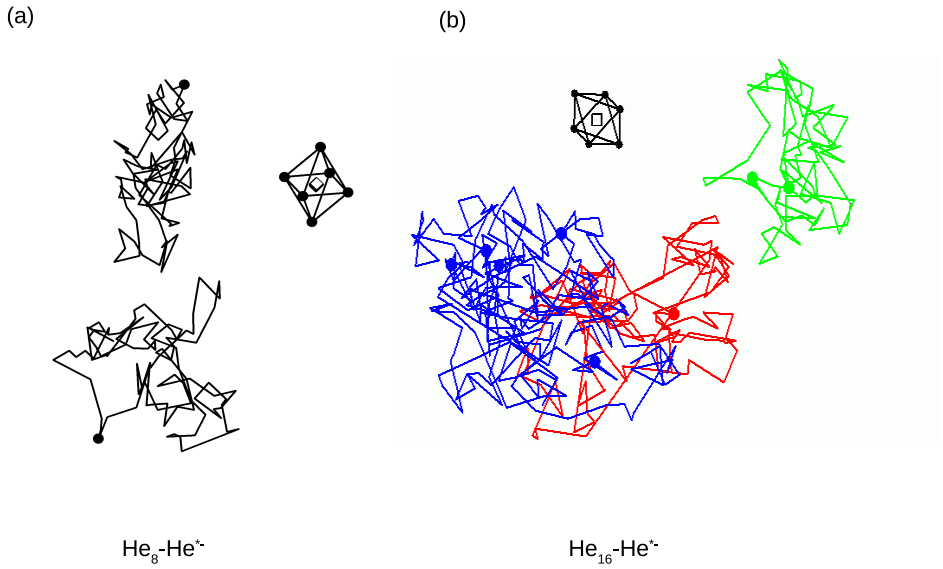

Figure 17. Snapshots from the PIMC simulation for the He_8-He^{*-} (left) and He_{16}-He^{*-} (right) clusters at $T = 0.4$ K. Exchange permutation paths of different lenghts: black is for one He atom; green is for two He atoms, red is for three atoms and blue for five.

effect is more noticeable as N increases as revealed in the comparison shown in Figure 17 between the situation for He_8-He^{*-} and He_{16}-He^{*-}. For the smallest cluster, paths for the two He atoms outside the central bipyramid do not mix thus indicating that they do not participate in exchange permutations. The 10 atoms surrounding the He_6-He^{*-} unit on the contrary are involved in permutation paths of different lenghts. In particular, for the PIMC calculation here performed at $T = 0.4$ K, paths of 2, 3 and 5 He atoms have been observed. As previously investigated for other systems, such as He clusters doped with SF_6, permutation movements in long paths becomes more likely as the size of the droplet increases: Thus, whereas for He_{23}-SF_6 PIMC calculations found about 7 He atoms exchanged in different chains, the number increases up to 59 for $N = 128$ [46]. In addition exchange effects were found relevant for He_{29}-SF_6 [69] at low temperatures such as $T = 0.625$ K, but almost non-existing at $T = 1.25$ K.

6. He_N-He_2^{*-}

There are not definitive conclusions regarding the precise pathway followed to form the molecular anion He_2^{*-}, that is, $He_2(1\sigma_g^2 1\sigma_u 2\sigma_g\, ^1\pi_4\, ^4\Pi_g)$. The low temperature regime within the helium clusters prevents the dimerization of a ground state He atom

and either He^* or He^{*-}, so the process needs to be initiated from an excited state of helium. The candidates are $He(1s2p\,^3P)$ and $He(1s3p\,^3P)$ [132], with excitation energies which, summed to the required penetration energy from the incident electron, yields formation energies for He_2^{*-} of 22.1 eV and 24.2 eV respectively [132, 133]. As opposed to the behaviour observed for the atomic anion discussed in Section 5, the molecular anion exhibits features of a heliophobic character which leads to its migration to the surface of the embedding helium droplet [132]. This trend excludes this species of the ionization process of impurities inside a helium enviroment due to the difficulties found for He_2^{*-} to move through the surrounding He atoms to interact with the corresponding dopant [135]. Authors of Ref. [135] reported *ab initio* energies for the $He(^1S)$–$He_2^{*-}(^4\Pi_g)$ interaction, calculated for different interparticle distances and angular orientations, while keeping the interparticle distance of He_2^{*-} at its equilibrium value of $\sim 1.2\mathring{A}$.

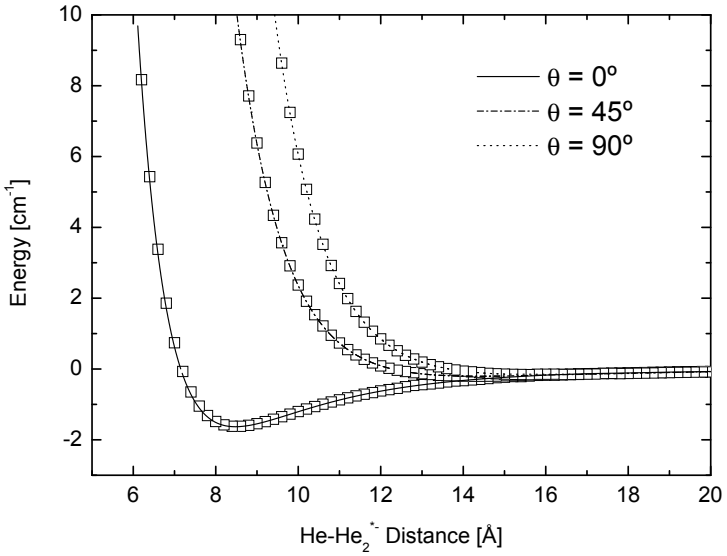

Figure 18. Potential energy interaction between He and He_2^{*-} for $\theta = 0°$, 45° and 90°, where θ is the angle between each He atom and the CM of the He_2^{*-} impurity. Points are *ab initio* results from Ref. [135] and lines correspond to the numerical fitting. Units of energy are cm^{-1} and distances are measured in $\mathring{A}$.

6.1. Calculation Details

The potential function describing the interaction between the He atoms and the He_2^{*-} anion depends both on the distance r_{He-X} and on the angle θ formed between the position vector of the He atom and the bond direction of the diatomic impurity:

$$V_{\text{He-He}_2^{*-}}(r,\cos\theta) = \begin{cases} \sum_{n=4}^{8} C_n(\cos\theta)/r^n & r > r_0 \\ \sum_{n=4}^{8} C_n(\cos\theta)/r_0^n & r \leq r_0 \end{cases} \tag{31}$$

Table 5. Values of the $a_{\ell n}$ coefficients for the expansion in Eq. (32) for the $V_{\text{He-He}_2^{*-}}(r, \cos\theta)$ potential describing the interaction between the diatomic anion impurity He_2^{*-} and the He atoms. See text for details.

	$\ell = 0$	$\ell = 1$	$\ell = 2$	$\ell = 3$	$\ell = 4$	$\ell = 5$
$a_{\ell 5}$ (10^7 Å^{-5} cm^{-1})	0.2055	0.1190	-1.2209	3.0799	-3.8827	1.7342
$a_{\ell 6}$ (10^9 Å^{-6} cm^{-1})	-0.0904	-0.0417	0.4457	-1.0453	1.2853	-0.5639
$a_{\ell 7}$ (10^{10} Å^{-7} cm^{-1})	0.1181	0.0494	-0.5404	1.2033	-1.4418	0.6200
$a_{\ell 8}$ (10^{10} Å^{-8} cm^{-1})	-0.4109	-0.1964	2.1065	-4.6991	5.4955	-2.3137

where a cutoff value of $r_0 = 6$ Å has been chosen and

$$C_n(\cos\theta) = \begin{cases} -\mathcal{C}_4 & n = 4 \\ \sum_{\ell=0}^{5} a_{\ell n} \cos^\ell \theta & n > 4 \end{cases} \tag{32}$$

where $\mathcal{C}_4 = 11363.2878$ Å^{-4} cm^{-1}. The values for the corresponding parameters in the expansion of Eq. (32) are shown in Table 5. The interparticle distance within the He_2^{*-} unit is assumed to correspond to the He–He* potential minimum equilibrium, ~ 1.2 Å(see Fig. 12).

The *ab initio* points obtained in Ref. [135] for three different values of the θ angle and the corresponding analytical fitting according to Eq. (31) can be seen in Figure 18. As opposed to other systems such as He_N–Rb_2 [30, 116] and He_N–Cs_2 [29, 142], the interaction between He and He_2^{*-} finds its most stable configuration in a linear structure along the diatom axis, $\theta \sim 0°$. In addition, other angular directions do not exhibit sufficiently deep potential wells to offer really stable alternative configurations for the He atoms added to the impurity. Despite the He–He_2^{*-} potential interaction supports at least one bound state for each possible θ direction (see Fig. 18)), the corresponding binding energies are quite small.

6.2. Results

The values of the energies, in cm^{-1}, for some He_N-He_2^{*-} clusters obtained by means of the PIMC method at $T = 0.4$ K [140] are shown in Table 6 in comparison with the estimates from the classical EA approach. This algorithm predicts energies which are strongly influenced by the He–He interaction, with a potential minimum about 4 times deeper than the equilibrium geometry of the He–X interaction. In fact the values of $E_{\text{EA}}^{(N)}$ for $N = 6, 8$ and 10 can be roughly approximated taking into account a certain number of He–He pairs (12, 19 and 26 respectively) separated by their equilibrium interparticle distance ~ 3 Å. In all cases, the remaining He atoms are located at larger distances (~ 4.8 Å).

Whereas the comparison between EA and CMC results at $T = 0.4$ K (not shown here) reveals differences which do not exceed 3 cm^{-1} [140], thus suggesting that thermal effects are not relevant, the PIMC method yields significantly weaker binding energies for the He_N-He_2^{*-} clusters. In order to obtain some insight regarding the stability of such systems we have performed a comparison with the corresponding pure Helium clusters, He_N, with values obtained by means of different MC approaches

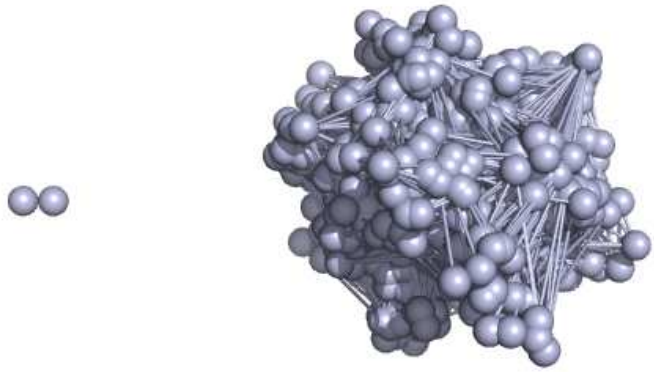

Figure 19. Snapshot from the PIMC simulation for the He_8-He_2^{*-} cluster at $T = 0.4$ K. The He_2^{*-} dopant remains outside the He droplet at the left.

Table 6. PIMC energies for the He_N-He_2^{*-} clusters, with $N = 6, 8$ and 10 at $T = 0.4$ K (second column) in comparison with estimates obtained by means of the EA (third column) and with values from VMC and DMC calculations of Ref. [143] for pure helium He_N clusters (fourth and fifth columns). Errors for the PIMC energies, in cm^{-1}, are given in parentheses.

N	PIMC	EA	He_N (VMC) [143]	He_N (DMC) [143]
6	-3.350 (0.365)	-98.765	-1.533	-1.647
8	-4.092 (0.324)	-156.248	-3.262	-3.568
10	-6.775 (0.229)	-220.485	-5.502	-6.015

as reported in Ref. [143]. Despite the $T = 0$ K character of these results and the fact that a slightly different He–He interaction potential was employed for the variational MC (VMC) and DMC calculations, the comparison shown in Table 6 reveals that the presence of the diatomic anion allows binding energies (obtained as differences between the DMC energies for the pure He_N clusters and the PIMC values for the corresponding doped systems) between 0.5 and ~ 2 cm^{-1} for the clusters under study.

The snapshot taken from the PIMC simulation performed for the He_8-He_2^{*-} cluster (see Fig. 19) indicates the preference of the impurity to remain outside the aggregate formed by the He atoms along the linear direction of the internal He_2^{*-} molecular axis,

as expected according to the He–X potential shown in Fig. 18. This configuration in which the diatomic anion is far to be embedded inside the cloud of solvating He atoms is also consistent with the previously reported heliophobic character of such dopant [132], which is supposed to migrate to the surface of the helium droplet.

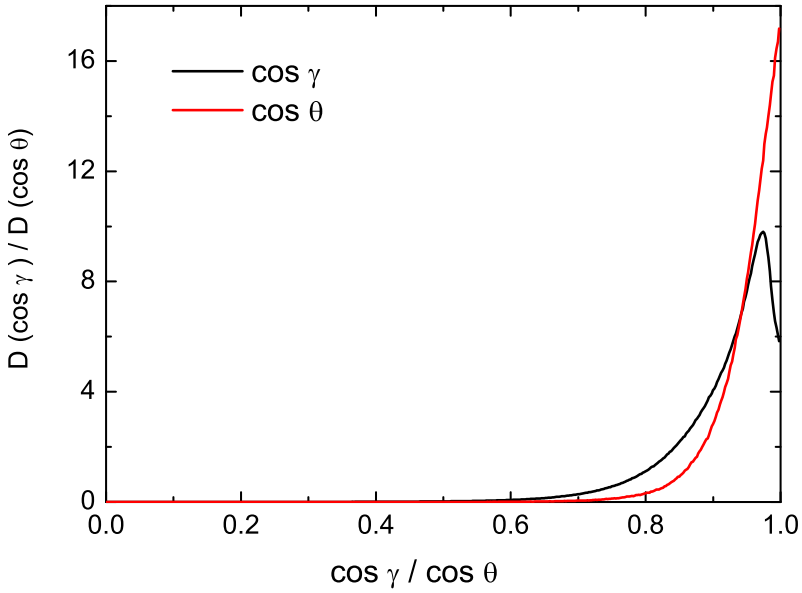

Figure 20. Angular probability densities for He_8-He_2^{*-} for $\cos\theta$ (red) and $\cos\gamma$ (black) obtained with the PIMC approach according to Eqs. (13) and (13), respectively, at $T = 0.4$ K. See text for details.

The analysis of the angular density probabilities leads to similar conclusions regarding the geometry of the cluster. Thus inspection of distributions for $\cos\gamma$ and $\cos\theta$ (see Eqs. (13) and (14) in previous sections) in the case of $N = 8$ shown in Figure 20 reveals peaks for $\mathcal{D}_8(\cos\gamma)$ and $\mathcal{D}_8(\cos\theta)$ close to 1. In particular, $\gamma \sim 0^\circ$ corresponds to short distances among the He atoms, an indication of an external He droplet, and $\theta \sim 0^\circ$ is consistent with the alignment of this helium cloud along the He_2^{*-} diatom axis.

The maxima of the probability densities for the different internal distances within the cluster shown in Figure 21, on the other hand, are consistent with a dopant located at far distances with respect to the solvating He droplet. That is in fact the possible explanation for the maximum of $\sim$ 12.5 Å found for $\mathcal{D}_8(\mathrm{r}_{\mathrm{He-He_2^{*-}}})$. This value exceeds to the average separation predicted by the EA method, which suggests the role of QM effects and certain independence of the PIMC calculation with respect to the potential energy minima. $\mathcal{D}_8(\mathrm{r}_{\mathrm{He-HeCM}})$ shows that the He atoms are located uniformly around the CM of the He_N structure with a maximum peak which in fact

is not far from the equilibrium distance of the $V_{\mathrm{He-He}}$ potential, much smaller than the observed He–He distance in $\mathcal{D}_8(\mathrm{r}_{\mathrm{He-He}})$ in Figure 21.

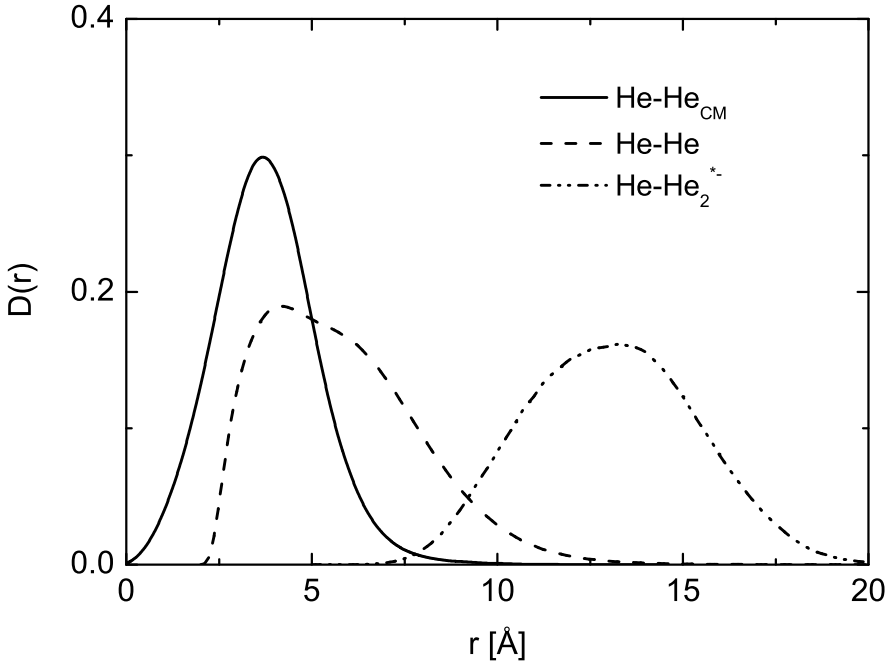

Figure 21. Radial probability densities for the He_8-He_2^{*-} cluster at $T = 0.4$ K for: (i) the He–He_{CM} of the He cluster distance (solid line); (ii) the He–He distance (dashed line) and (iii) the He–He_2^{*-} dopant distance (dashed-dotted line) obtained with the PIMC approach. Units are Å.

7. Conclusions

Doped helium clusters have been the subject of numerous studies over the years. In this work we have reviewed PIMC investigations on He clusters doped with Ca, Rb_2, He^{*-} and He_2^{*-} performed by our group. A detailed analysis of both geometries and energies of clusters formed with these dopants attached to droplets of up to 40 He atoms is presented. The variety of chosen impurities, both neutral and ionic species and, atomic and diatomic systems, offers the possibility to tackle different issues of interest. The specific characteristics of the interaction potentials, which in some of the cases are derived from analytical fittings to *ab initio* quantum calculated energies, are correlated with intrisic properties such as energetics, geometries and the precise position of the impurity with respect to the helium droplet. The application of the PIMC approach with the explicit inclusion of internal degrees of freedom of the dopant is discussed for the case of Rb_2. In addition, exchange permutation symmetry

for the He atoms is taken into account for the He^{*-} impurity, whose mobility within the helium environment is assumed to play a key role in ionization processes inside this kind of clusters. The effect of the dopant on the superfluidity of the droplet has not been investigated here because in most of the cases considered in this review the impurity is usually located outside the helium cluster with little influence on it.

8. Acknowledgments

This work has been supported by MICINN Grant No. FIS2011-29596-C02-01 and FIS2014-51933-P.

References

[1] J. A. Northby, J. Chem. Phys. **115** (22), 10065–10077 (2001).
[2] P. Toennies and A. F. Vilesov, Annu. Rev. Phys. Chem. **49**, 1–41 (1998).
[3] C. Callegari, K. K. Lehmann, R. Schmied, and G. Scoles, J. Chem. Phys. **115** (22), 10090–10110 (2001).
[4] F. Stienkemeier and A. F. Vilesov, J. Chem. Phys. **115** (22), 10119–10137 (2001).
[5] J. P. Toennies and A. F. Vilesov, Angew. Chem. Int. Edit. **43** (20), 2622–2648 (2004).
[6] M. Y. Choi, G. E. Douberly, T. M. Falconer, W. K. Lewis, C. M. Lindsay, J. M. Merritt, P. L. Stiles, and R. E. Miller, Int. Rev. Phys. Chem. **25**, 15–75 (2006).
[7] M. Mudrich and F. Stienkemeier, Inter. Rev. Phys. Chem. **33**, 301 (2014).
[8] C. Callegari and W. E. Ernst, in *Handbook of High Resolution Spectroscopy*, edited by F. Merkt and M. Quack, *John Wiley and Sons*, Vol. 3 (Chichester 2011), pp. 1551–1594.
[9] S. Yang and A. M. Ellis, Chem. Soc. Rev. **42**, 472–484 (2013).
[10] F. Stienkemeier and K. K. Lehmann, J. Phys. B: Atom., Mol. Opt. Phys. **39** (8), R127 (2006).
[11] M. Barranco, R. Guardiola, S. Hernández, R. Mayol, J. Navarro, and M. Pi, J. Low Temp. Phys. **142** (1-2), 1–81 (2006).
[12] S. Goyal, D. L. Schutt, and G. Scoles, Phys. Rev. Lett. **69**, 933–936 (1992).
[13] M. Hartmann, R. E. Miller, J. P. Toennies, and A. Vilesov, Phys. Rev. Lett. **75**, 1566 (1995).
[14] S. Grebenev, J. P. Toennies, and A. F. Vilesov, Science **279** (5359), 2083–2086 (1998).
[15] K. Nauta and R. E. Miller, Science **283** (5409), 1895–1897 (1999).
[16] Y. Kwon and K. B. Whaley, J. Chem. Phys. **114** (7), 3163–3169 (2001).
[17] J. Tang, Y. Xu, A. R. W. McKellar, and W. Jäger, Science **297** (5589), 2030–2033 (2002).
[18] T. Zeng and P. N. Roy, Rep. Prog. Phys. **77** (4), 046601 (2014).
[19] A. Bartelt, J. D. Close, F. Federmann, N. Quaas, and J. P. Toennies, Phys. Rev. Lett. **77** (17), 3525 (1996).
[20] A. Ancilotto, E. Cheng, M. W. Cole, and F. Toigo, Z. Phys. B: Condens. Matter **98**, 323 (1995).
[21] F. Stienkemeier, J. Higgins, C. Callegari, S. I. Karnorsky, W. E. Ernst, and G. Scoles, Z. Phys. D **38**, 253 (1996).
[22] A. Nakayama and K. Yamashita, J. Chem. Phys. **114** (2), 780 (2001).
[23] A. Bartelt, J. D. Close, F. Federmann, K. Hoffman, N. Quaas, and J. Toennies, Z. Phys. D: At. Mol. Clusters **1**, 1 (1997).
[24] F. Stienkemeier, F. Meier, and H. O. Lutz, J. Chem. Phys. **107** (24), 10816 (1997).
[25] F. Stienkemeier, F. Meier, and H. O. Lutz, Eur. Phys. J. D **9** (1), 313 (1999).
[26] J. Reho, U. Merker, M. R. Radcliff, K. K. Lehmann, and G. Scoles, J. Chem. Phys. **112** (19), 8409 (2000).
[27] J. Navarro, D. Mateo, M. Barranco, and A. Sarsa, J. Chem. Phys. **136** (5), 054301 (2012).
[28] S. Bovino, E. Coccia, E. Bodo, D. Lopez-Durán, and F. A. Gianturco, J. Chem. Phys. **130** (22), 224903 (2009).
[29] R. Pérez de Tudela, D. López-Durán, T. González-Lezana, G. Delgado-Barrio, P. Villarreal, F. A. Gianturco, and E. Yurtsever, J. Phys. Chem. A **115** (25), 6892 (2011).
[30] G. Guillon, A. Zanchet, M. Leino, A. Viel, and R. E. Zillich, J. Phy. Chem. A **115** (25), 6918 (2011).
[31] D. López-Durán, R. Rodríguez-Cantano, T. González-Lezana, G. Delgado-Barrio, P. Villarreal, E. Yurtsever, and F. A. Gianturco, J. Phys. Cond. Matt. **24** (10), 104014 (2012).
[32] F. Ancilotto, P. Lerner, and M. Cole, J. Low Temp. Phys. **101** (5-6), 1123 (1995).
[33] C. Douketis, G. Scoles, S. Marchetti, M. Zen, and A. J. Thakkar, J. Chem. Phys. **76** (6), 3057–3063 (1982).
[34] D. J. Funk, W. H. Breckenridge, J. Simons, and G. Chalasiński, J. Chem. Phys. **91**

(2), 1114–1120 (1989).
[35] E. Czuchaj, F. Rebentrost, H. Stoll, and H. Preuss, Chem. Phys. Lett. **182** (2), 191 (1991).
[36] R. Pérez de Tudela, P. Barragán, A. Valdés, and R. Prosmiti, J. Phys. Chem. A **118** (33), 6492–6500 (2014).
[37] L. Delgado-Tellez, A. Valdés, R. Prosmiti, P. Villarreal, and G. Delgado-Barrio, Int. J. Quant. Chem. **112** (17), 2971–2975 (2012).
[38] L. García-Gutierrez, L. Delgado-Tellez, A. Valdés, R. Prosmiti, P. Villarreal, and G. Delgado-Barrio, J. Phys. Chem. A **113** (19), 5754–5762 (2009).
[39] N. F. Aguirre, P. Villarreal, G. Delgado-Barrio, A. O. Mitrushchenkov, and M. P. de Lara-Castells, Phys. Chem. Chem. Phys. **15**, 10126–10140 (2013).
[40] M. P. de Lara-Castells, R. Prosmiti, G. Delgado-Barrio, D. López-Durán, P. Villarreal, F. A. Gianturco, and J. Jellinek, Phys. Rev. A **74**, 053201 (2006).
[41] T. González-Lezana, M. I. Hernández, G. Delgado-Barrio, A. A. Buchachenko, and P. Villarreal, J. Chem. Phys. **105**, 7454 (1996).
[42] A. A. Buchachenko, R. Prosmiti, C. Cunha, G. Delgado-Barrio, and P. Villarreal, J. Chem. Phys. **117** (13), 6117–6120 (2002).
[43] F. Dalfovo, R. Mayol, M. Pi, and M. Barranco, Phys. Rev. Lett. **85**, 1028–1031 (2000).
[44] K. Szalewicz, Int. Rev. Phys. Chem. **27** (2), 273–316 (2008).
[45] D. M. Ceperley and L. Mitas, Adv. Chem. Phys. **93**, 1 (1996).
[46] Y. Kwon, P. Huang, M. V. Patel, D. Blume, and K. B. Whaley, J. Chem. Phys. **113** (16), 6469 (2000).
[47] S. Moroni, A. Sarsa, S. Fantoni, K. E. Schmidt, and S. Baroni, Phys. Rev. Lett. **90**, 143401 (2003).
[48] A. Viel and K. B. Whaley, J. Chem. Phys. **115** (22), 10186–10198 (2001).
[49] P. Cazzato, S. Paolini, S. Moroni, and S. Baroni, J. Chem. Phys. **120** (19), 9071–9076 (2004).
[50] F. Paesani, F. Gianturco, and K. Whaley, Europhys. Lett. **56** (5), 658 (2001).
[51] F. Paesani, F. A. Gianturco, and K. B. Whaley, J. Chem. Phys. **115** (22), 10225–10238 (2001).
[52] F. Paesani, A. Viel, F. A. Gianturco, and K. B. Whaley, Phys. Rev. Lett. **90**, 073401 (2003).
[53] S. Moroni, N. Blinov, and P. N. Roy, J. Chem. Phys. **121** (8), 3577–3581 (2004).
[54] D. López-Durán, M. P. de Lara-Castells, G. Delgado-Barrio, P. Villarreal, C. Di Paola, F. A. Gianturco, and J. Jellinek, Phys. Rev. Lett. **93**, 053401 (2004).
[55] M. P. de Lara-Castells, D. López-Durán, G. Delgado-Barrio, P. Villarreal, C. Di Paola, F. A. Gianturco, and J. Jellinek, Phys. Rev. A **71**, 033203 (2005).
[56] D. López-Durán, M. P. de Lara-Castells, G. Delgado-Barrio, P. Villarreal, C. Di. Paola, F. A. Gianturco, and J. Jellinek, J. Chem. Phys. **121** (7), 2975–2984 (2004).
[57] M. P. de Lara-Castells, G. Delgado-Barrio, P. Villarreal, and A. O. Mitrushchenkov, J. Chem. Phys. **125** (22) (2006).
[58] M. P. de Lara-Castells, P. Villarreal, G. Delgado-Barrio, and A. O. Mitrushchenkov, J. Chem. Phys. **131** (19), 194101 (2009).
[59] S. Stringari and J. Treiner, J. Chem. Phys. **87** (8), 5021–5027 (1987).
[60] A. Hernando, R. Mayol, M. Pi, M. Barranco, F. Ancilotto, O. Bünermann, and F. Stienkemeier, J. Phys. Chem. A **111** (31), 7303 (2007).
[61] D. M. Ceperley and E. L. Pollock, Phys. Rev. Lett. **56**, 351 (1986).
[62] P. Sindzingre, M. L. Klein, and D. M. Ceperley, Phys. Rev. Lett. **63**, 1601–1604 (1989).
[63] D. M. Ceperley, Rev. Mod. Phys. **67** (2), 279 (1995).
[64] F. Paesani, Y. Kwon, and K. B. Whaley, Phys. Rev. Lett. **94**, 153401 (2005).
[65] F. Paesani and K. B. Whaley, J. Chem. Phys. **121** (11), 5293–5311 (2004).
[66] N. Blinov, X. Song, and P. N. Roy, J. Chem. Phys. **120** (13), 5916 (2004).
[67] P. Huang and K. B. Whaley, J. Chem. Phys. **117** (24), 11244–11264 (2002).
[68] Y. Kwon and K. Birgitta Whaley, Phys. Rev. Lett. **83**, 4108–4111 (1999).

[69] Y. Kwon, D. M. Ceperley, and K. B. Whaley, J. Chem. Phys. **104** (6), 2341 (1996).
[70] R. Pérez de Tudela, M. Marquez-Mijares, T. González-Lezana, O. Roncero, S. Miret-Artés, G. Delgado-Barrio, and P. Villarreal, J. Chem. Phys. **132** (24), 244303 (2010).
[71] R. Rodríguez-Cantano, D. López-Durán, R. Pérez de Tudela, T. González-Lezana, G. Delgado-Barrio, P. Villarreal, and F. A. Gianturco, Comp. Theor. Chem. **990** (0), 106 (2012).
[72] F. F. Abraham and J. Q. Broughton, Phys. Rev. Lett. **59**, 64–67 (1987).
[73] M. E. Pierce and E. Manousakis, Phys. Rev. Lett. **83**, 5314–5317 (1999).
[74] F. Calvo, J. Phys. Chem. A **119**, 5959 (2015).
[75] B. E. Clements, J. L. Epstein, E. Krotscheck, and M. Saarela, Phys. Rev. B **48**, 7450–7470 (1993).
[76] F. Dalfovo, A. Lastri, L. Pricaupenko, S. Stringari, and J. Treiner, Phys. Rev. B **52**, 1193–1209 (1995).
[77] G. Zimmerli, G. Mistura, and M. H. W. Chan, Phys. Rev. Lett. **68**, 60–63 (1992).
[78] B. J. Berne and D. Thirumalai, Annu. Rev. Phys. Chem. **37** (1), 401–424 (1986).
[79] J. A. Barker, J. Chem. Phys. **70** (6), 2914 (1979).
[80] M. F. Herman, E. J. Bruskin, and B. J. Berne, J. Chem. Phys. **76** (10), 5150 (1982).
[81] K. R. Glaesemann and L. E. Fried, J. Chem. Phys. **116** (14), 5951 (2002).
[82] R. Rodríguez-Cantano, R. Pérez de Tudela, D. López-Durán, T. González-Lezana, F. A. Gianturco, G. Delgado-Barrio, and P. Villarreal, Eur. Phys. J. D **67** (6), 119 (2013).
[83] Z. Li, L. Wang, H. Ran, D. Xie, N. Blinov, P. N. Roy, and H. Guo, J. Chem. Phys. **128** (22), 224513 (2008).
[84] D. Marx and M. Müser, J. Phys.: Condens. Mat. **11**, 117 (1999).
[85] R. E. Zillich, J. M. Mayrhofer, and S. A. Chin, J. Chem. Phys. **132** (4), 044103 (2010).
[86] E. G. Noya, C. Vega, and C. McBride, J. Chem. Phys. **134**, 054117 (2011).
[87] E. G. Noya, L. Ses, R. Ramírez, C. McBride, and C. Vega, Mol. Phys. **109**, 149 (2011).
[88] M. Iwamatsu, Comput. Phys. Commun. **142**, 214–218 (2001).
[89] N. Metropolis, A. W. Rosenbluth, M. N. Rosenbluth, A. Teller, and T. E., J. Chem. Phys. **21**, 1087 (1953).
[90] D. M. Ceperley and E. L. Pollock, Phys. Rev. B **39** (4), 2084 (1989).
[91] M. Sprik, M. L. Klein, and D. Chandler, Phys. Rev. B **31**, 4234 (1985).
[92] J. E. Cuervo and P. N. Roy, J. Chem. Phys. **125** (12), 124314 (2006).
[93] R. A. Aziz and M. J. Slaman, J. Chem. Phys. **94** (12), 8047 (1991).
[94] U. Kleinekathöfer, Chem. Phys. Lett. **324** (56), 403 (2000).
[95] C. C. Lovallo and M. Klobukowski, J. Chem. Phys. **120** (1), 246 (2004).
[96] D. D. Yang, P. Li, and K. T. Tang, J. Chem. Phys. **131** (15), 154301 (2009).
[97] F. Stienkemeier, K. Meier, K. Stark, and H. Lutz, Farad. Discuss. **108**, 212 (1997).
[98] E. Czuchaj, M. Krośnicki, and H. Stoll, Chem. Phys. **292** (1), 101 (2003).
[99] R. J. Hinde, J. Phys. B: Atom. Mol. Opt. Phys. **36** (14), 3119 (2003).
[100] D. López-Durán, R. Rodríguez-Cantano, T. González-Lezana, G. Delgado-Barrio, P. Villarreal, and F. A. Gianturco, Eur. Phys. J. D **66** (7), 1 (2012).
[101] D. López-Durán, R. Rodríguez-Cantano, T. González-Lezana, G. Delgado-Barrio, P. Villarreal, and F. A. Gianturco, Phys. Rev. A **86** (2), 022501 (2012).
[102] O. Bünermann, M. Dvorak, F. Stienkemeier, A. Hernando, R. Mayol, M. Pi, M. Barranco, and F. Ancilotto, Phys. Rev. B **79** (21), 214511 (2009).
[103] A. Hernando, M. Barranco, R. Mayol, M. Pi, and M. Krośnicki, Phys. Rev. B **77** (2), 024513 (2008).
[104] R. Guardiola, J. Navarro, D. Mateo, and M. Barranco, J. Chem. Phys. **131** (17), 174110 (2009).
[105] Y. Moriwaki and N. Morita, Eur. Phys. J. D **33**, 323 (2005).
[106] F. Ancilotto, M. Barranco, and M. Pi, Phys. Rev. Lett. **91** (10), 105302 (2003).
[107] R. Rodríguez-Cantano, T. González-Lezana, P. Villarreal, D. López-Durán, F. A. Gianturco, and G. Delgado-Barrio, Int. J Quant. Chem. **114** (19), 1318–1326 (2014).

[108] K. T. Tang and J. P. Toennies, J. Chem. Phys. **80** (8), 3726–3741 (1984).
[109] J. M. Standard and P. R. Certain, J. Chem. Phys. **83** (6), 3002–3008 (1985).
[110] K. T. Tang and J. Peter Toennies, Surf. Sci. Lett. **279** (3), L203–L206 (1992).
[111] J. Boronat, K. Sakkos, E. Sola, and J. Casulleras, J. Low Temp. Phys. **148** (5-6), 845–849 (2007).
[112] R. A. Aziz, F. R. McCourt, and C. C. Wong, Molecular Physics **61** (6), 1487–1511 (1987).
[113] J. Higgins, C. Callegari, J. Reho, F. Stienkemeier, W. E. Ernst, M. Gutowski, and G. Scoles, J. Phys. Chem. A **102** (26), 4952–4965 (1998).
[114] P. Claas, G. Droppelmann, C. P. Schulz, M. Mudrich, and F. Stienkemeier, J. Phys. Chem. A **111** (31), 7537–7541 (2007).
[115] W. E. Ernst, R. Huber, S. Jiang, R. Beuc, M. Movre, and G. Pichler, J. Chem. Phys. **124** (2) (2006).
[116] R. Rodríguez-Cantano, D. López-Durán, T. González-Lezana, G. Delgado-Barrio, P. Villarreal, E. Yurtsever, and F. A. Gianturco, J. Phys. Chem. A **116** (10), 2394 (2012).
[117] O. Allard, J. Nagl, G. Auböck, C. Callegari, and W. Ernst, J. Phys. B: Atmos. Mol. Opt. Phys. **39**, S1169 (2006).
[118] M. Mudrich, F. Stienkemeier, G. Droppelmann, P. Claas, and C. P. Schultz, Phys. Rev. Lett. **100**, 023401 (2008).
[119] G. Auböck, M. Aymar, O. Dulieu, and W. E. Ernst, J. Chem. Phys. **132** (5), 054304 (2010).
[120] M. Mudrich, P. Heister, T. Hippler, C. Giese, O. Dulieu, and F. Stienkemeier, Phys. Rev. A **80**, 042512 (2009).
[121] C. P. Schulz, P. Claas, D. Schumacher, and F. Stienkemeier, Phys. Rev. Lett. **92**, 013401 (2004).
[122] F. R. Brühl, R. A. Miron, and W. E. Ernst, J. Chem. Phys. **115** (22), 10275–10281 (2001).
[123] G. Auböck, J. Nagl, C. Callegari, and W. E. Ernst, J. Phys. Chem. A **111** (31), 7404–7410 (2007).
[124] J. Lozeille, A. Fioretti, C. Gabbanini, Y. Huang, H. K. Pechkis, D. Wang, P. L. Gould, E. E. Eyler, W. C. Stwalley, M. Aymar, and O. Dulieu, Eur. Phys. J. D **39**, 261 (2006).
[125] G. Guillon, A. Viel, and J. M. Launay, J. Chem. Phys. **136** (17), 174307 (2012).
[126] R. Rodríguez-Cantano, T. González-Lezana, R. Prosmiti, G. Delgado-Barrio, P. Villarreal, and J. Jellinek, J. Chem. Phys. **142** (16), 164304 (2015).
[127] A. Viel and J. M. Launay, J. Phys. Chem. A **118** (33), 6529–6535 (2014).
[128] S. Miura, J. Chem. Phys. **126**, 114308 (2007).
[129] E. Svensson, V. Sears, A. D. B. Woods, and P. Martel, Phys. Rev. B **21**, 3638 (1980).
[130] D. López-Durán, R. P. de Tudela, R. Rodríguez-Cantano, T. González-Lezana, M. P. de Lara-Castells, G. Delgado-Barrio, and P. Villarreal, Phys. Scripta **84** (2), 028107 (2011).
[131] U. Henne and J. P. Toennies, J. Chem. Phys. **108** (22), 9327–9338 (1998).
[132] A. Mauracher, M. Daxner, J. Postler, S. E. Huber, S. Denifl, P. Scheier, and J. P. Toennies, J. Phys. Chem. Lett. **5** (14), 2444–2449 (2014).
[133] S. E. Huber and A. Mauracher, J. Phys. Chem. A **118** (33), 6642–6647 (2014).
[134] K. Martini, J. Toennies, and C. Winkler, Chem. Phys. Lett. **178** (4), 429 – 434 (1991).
[135] S. E. Huber and A. Mauracher, Mol. Phys. **112** (5-6), 794–804 (2014).
[136] C. G. Kuper, Phys. Rev. **122**, 1007–1011 (1961).
[137] J. Poitrenaud and F. I. B. Williams, Phys. Rev. Lett. **29**, 1230–1232 (1972).
[138] G. G. Ihas and T. M. Sanders, Phys. Rev. Lett. **27**, 383–386 (1971).
[139] Y. K. Bae, M. J. Coggiola, and J. R. Peterson, Phys. Rev. Lett. **52**, 747–750 (1984).
[140] R. Rodríguez-Cantano, T. González-Lezana, P. Villarreal, and F. A. Gianturco, J. Chem. Phys. **142** (10), 104303 (2015).
[141] Y. K. P. Huang and K. B. Whaley, in *Microscopic Approaches to Quantum Liquids in Confined Geometries*, edited by E. Krotscheck and J. Navarro, , Vol. 4, p. 91.

[142] R. Prosmiti, G. Delgado-Barrio, P. Villarreal, E. Yurtsever, E. Coccia, and F. A. Gianturco, J. Phys. Chem. A **113** (52), 14718–14729 (2009).
[143] M. Lewerenz, J. Chem. Phys. **106** (11), 4596 (1997).